MATHEMATICAL MODELING, ANALYSIS, AND SIMULATION OF

CHOLERA DYNAMICS

By

Chayu Yang

Jin Wang
Professor of Mathematics
(Chair)

Lingju Kong
Professor of Mathematics
(Committee Member)

Andrew Ledoan
Associate Professor of Mathematics
(Committee Member)

Yu Liang
Associate Professor of Computer Science
(Committee Member)

MATHEMATICAL MODELING, ANALYSIS, AND SIMULATION OF CHOLERA DYNAMICS

By

Chayu Yang

A Dissertation Submitted to the Faculty of The University of Tennessee at Chattanooga in Partial Fulfillment of the Requirements of the Degree of Doctor of Philosophy in Computational Science: Applied Mathematics

The University of Tennessee at Chattanooga
Chattanooga, Tennessee

August 2020

ABSTRACT

We propose multiple models to investigate the transmission dynamics of cholera. At first, we consider the intrinsic growth of cholera bacteria in cholera transmission and find that the regular threshold dynamics take place if the intrinsic growth is logistic; there are multiple endemic equilibria if the growth exhibits Allee effects, which may lead to backward bifurcation and forward hysteresis. In addition, we introduce a multi-scale modeling framework. At the population level, a Susceptible-Infected-Recovered (SIR) model for the between-host transmission of cholera is employed. At the individual host level, the evolution of the pathogen within the human body is incorporated. The between-host and within-host dynamics are connected through an environmental equation that characterizes the growth of the pathogen and its interaction with the hosts outside the human body. We put a special emphasis on the within-host dynamics by making a distinction for each individual host. We conduct both mathematical analysis and numerical simulation for the model in order to explore various scenarios associated with cholera transmission and to better understand the complex, multi-scale disease dynamics. Finally, we analyze the impact of available medical resources on cholera transmission by taking a realistic case: Yemen cholera outbreak during 2017-2018. By fitting our simulation results to the epidemic data published by the World Health Organization (WHO), we find that different levels of disease prevalence and severity are linked to different geographical regions in this country and that cholera prevention and intervention efforts should be implemented strategically with respect to these regions in Yemen.

ACKNOWLEDGEMENT

I am grateful to the Department of Mathematics and the College of Engineering and Computer Science of the University of Tennessee at Chattanooga for the support they always provide to me. I would like to express my great appreciation to my supervisor, professor Jin Wang, for his continued concern and advice throughout the research process and I also offer my sincere thanks to each of my graduate committee members for their valuable suggestions and help.

TABLE OF CONTENTS

ABSTRACT iii

ACKNOWLEDGEMENT iv

LIST OF FIGURES vi

LIST OF TABLES vii

1 INTRODUCTION 1

2 INTRINSIC GROWTH OF BACTERIA IN CHOLERA DYNAMICS 8
2.1 Logistic growth 8
2.1.1 Nontrivial equilibria 10
2.1.2 Stabilities 12
2.2 Growth with Allee effects 18
2.2.1 Endemic equilibria analysis 19
2.2.2 Simulation results and bifurcation diagrams 28
2.3 Discussion 33

3 MULTI-SCALE CHOLERA MODEL 36
3.1 Model formulation 36
3.2 Separation of scales 38
3.3 Basic reproduction number 39
3.4 Equilibria analysis 42
3.5 Numerical simulation 48
3.6 Discussion 51

4 CHOLERA MODEL INCORPORATING MEDICAL RESOURCES 52
4.1 Model formulation and analysis 52
4.1.1 Basic reproduction number 53
4.1.2 Equilibria analysis 54
4.2 Numerical results 64
4.3 Discussion 73

5 CONCLUSION 75

REFERENCES 77

VITA 82

LIST OF FIGURES

2.1 An illustration showing the function $T(B)$ has at least one root in $(0, b)$..... 22

2.2 An illustration showing the function $T(B)$ is decreasing in $(0, b)$..... 23

2.3 An illustration showing the function $T(B)$ has exactly one root in (y, b)..... 24

2.4 The intersections of $I = q(B)$ and $I = g(B)$ in (0, b) when $\mathcal{R}_0 > 1$..... 25

2.5 The intersections of $I = q(B)$ and $I = g(B)$ in (0, b) when $\mathcal{R}_0 < 1$..... 27

2.6 Typical solution orbits of B versus time when $T''(0) \leq 0$..... 29

2.7 Typical solution orbits of B versus time when $T''(0) > 0$..... 29

2.8 A backward bifurcation occurs at $\mathcal{R}_0 = 1$ when $T''(0) \leq 0$..... 30

2.9 A forward hysteresis occurs when $T''(0) > 0$..... 30

2.10 Bifurcation diagrams for $T''(0) > 0$ with varied intrinsic growth rate r..... 31

2.11 Typical bifurcation diagrams for the modified model..... 32

3.1 A typical phase portrait for I versus B when $\mathcal{R}_0 < 1$..... 49

3.2 A typical phase portrait for I versus S when $R_1 > 1$..... 50

3.3 Z_i versus time for $i = 1, 5, 10$..... 50

4.1 Curve fitting for Yemen from April 2017 to May 2018..... 66

4.2 Long-term behavior of the infection in Yemen..... 67

4.3 Curve fittings for Al Hudaydah and Taizz..... 69

4.4 Curve fittings for Al Jawf and Sa'ada..... 71

4.5 Comparison with two hypothetical scenarios: $M = 0$ and $M = 1$..... 71

LIST OF TABLES

3.1 Model parameters and values (p=person, d=days)..... 49

4.1 The NMSE for the cholera data fitting of Yemen and its four governorates..... 67

4.2 Parameter values and confidence intervals for Yemen..... 68

4.3 Parameter values and confidence intervals for Al Hudaydah..... 70

4.4 Parameter values and confidence intervals for Taizz..... 70

4.5 Parameter values and confidence intervals for Al Jawf..... 72

4.6 Parameter values and confidence intervals for Sa'ada..... 73

4.7 The values of $M_0, \mathcal{R}_{01}, \mathcal{R}_{02}$, and $\mathcal{R}_0$ in four governorates..... 73

CHAPTER 1

INTRODUCTION

Cholera, an ancient infectious disease, is caused by several strains of the bacterium *Vibrio Cholerae*. The typical symptom is large amounts of watery diarrhea that lasts a few days. Vomiting and muscle cramps may also occur. It is spread mostly by unsafe water and unsafe food which have been contaminated with bacteria. It also can be transmitted from human-to-human contacts such as shaking hands or eating food prepared by infected individuals [27, 40]. Currently, in its seventh pandemic, cholera continues devastating populations in developing countries, particularly those places where sanitation facilities and access to clean drinking water are limited. Large-scale cholera outbreaks in recent years, such as those in Zimbabwe (2008-2009, with nearly 100,000 reported cases), Haiti (2010-2012, with 545,000 reported cases), and Yemen (2016-2018, with suspected cases exceeding 1 million), have received worldwide attention.

Mathematical modeling, analysis, and simulation have long provided useful insight into epidemiology. In order to understand the fundamental mechanisms in cholera transmission and to quantify effective prevention and intervention strategies, a large number of mathematical models have been published for the dynamics of cholera transmission [3, 9, 12, 19, 27, 40, 41, 44, 47, 52, 53, 56–58]. Many of these models included both direct and indirect transmission pathways in order to better characterize the transmission pattern of cholera infections.

One major limitation of current modeling studies in cholera transmission, however, is that the intrinsic dynamics of the bacterium are poorly addressed, leading to incomplete, and often, inadequate, understanding of the bacterium evolution and its impact on disease transmission and spread. For example, a standard assumption in the majority of

cholera models, based on an early theory in cholera ecology [22], is that the Vibrios (i.e., *Vibrio Cholerae*) cannot sustain themselves in the absence of human contribution; e.g., shedding from infected individuals and inflow from contaminated sewage. The assumption allows a simple, often linear, representation of the rate of change for the bacterial density: a positive contribution from the infected human population, and a negative contribution due to the natural death of the Vibrios. Such a representation considerably simplifies the mathematical analysis. Unfortunately, there has been strong evidence in recent ecological studies that the Vibrios can independently survive and multiply in various aquatic environments, including freshwater, estuaries, and seawater [7, 13, 18, 20]. These ecological findings demand new modeling efforts toward better understanding the intrinsic dynamics of cholera diseases and the connection between their environmental persistence and disease outbreaks.

Second, most mathematical modeling studies are concerned with the between-host transmission and spread at the population level, and very little effort has been devoted to the within-host dynamics of cholera, partly due to the complication of the biochemical and genetic interactions that occur within the human body. As a consequence, some important information in cholera dynamics is missing from such studies; for example, how does the virulence of the pathogens (i.e., the vibrios) change inside the human body, and how does the within-host evolution of the pathogens impact the population-level disease transmission? In a recent study [60], the authors proposed a within-host cholera model to describe the evolution of vibrios and their interaction with the cholera-toxin phage (a virus that is important in the pathogenesis of *Vibrio Cholerae*) within the human body. The connection between the within-host dynamics and the between-host disease transmission, however, was not discussed. A multi-scale cholera model, that considers the between-host and within-host interactions, was proposed in [59]. In that work, the within-host dynamics take a simplistic form: a single equation characterizing the increased toxicity of the vibrios within an "average" (or typical) infected individual. Distinctions among different human hosts were not considered. We also mention that there have been several mathematical models published for the immuno-epidemiological

dynamics of other types of diseases; for example, a recent study on malaria can be found in [10].

In order to shed light on those important aspects of cholera disease epidemiology, we will first incorporate nonlinear dynamics terms into the bacterium evolution equation and focus on two types of intrinsic bacterial dynamics: quadratic growth and cubic growth. The quadratic growth, more commonly referred to as the logistic growth [29], is probably the most popular model to describe population changes, ranging from macroscopic to microscopic organisms. Essentially, this model introduces a threshold for the total population, known as the carrying capacity, so that a population would exponentially grow initially but then stabilize at the carrying capacity. The model could reflect realistic constraints (such as lack of resources) on population growth. A significant departure from the logistic growth pattern, the cubic growth model is known to introduce Allee effects. An Allee effect refers to a correlation between individual fitness and population density [1,2]. Particularly, a strong Allee effect describes a population that exhibits positive growth at intermediate population density but declines when the population density is either too low or too high. Allee effects have been well documented and extensively studied for the growth dynamics among animal populations [1,14,33]; related mathematical modeling work includes, for example, [16,17,23,32,50]. There are relatively few studies for Allee effects in populations of microorganisms such as bacteria and parasites. Kadam and Velicer [31] reported laboratory measurements of the bacterium *Myxococcus xanthus* and found that it sporulates less efficiently at lower population densities and produces no spores at all below a minimum threshold density. Li et al. [35] demonstrated that bacterial populations in high-density biofilms are better able to generate a coordinated protective response against highly acidic conditions than are populations at low density, thus promoting the survival of the microbial species. Ji et al. [30] observed that a minimum population density is typically needed for some pathogenic microbes to initiate the expression of virulence factors necessary for the establishment of successful infections. In addition, Smith et al. [49] investigated Allee effects on the bacterial spread and survival through the engineered bacterium *Escherichia coli*. In all these studies, it is observed

that a minimal density, known as the Allee threshold, is required to initiate positive population development. Given the significance of cholera infections, the complications of their related dynamics, and the experimental evidence of the nontrivial growth patterns of the bacterium, it is worthwhile to mathematically explore the details of the intrinsic bacterial dynamics and the impact on cholera disease transmission.

In addition, we will try to extend the work in [60], in an effort to fill the knowledge gap in linking the between-host and within-host cholera dynamics while taking into account the heterogeneity among different individual hosts. In this modeling framework, we distinguish two types of vibrios relevant to cholera infection: the environmental vibrios and the human vibrios [59, 60], based on their toxicity, or infectivity. The environmental vibrios have relatively low infectivity, whereas the human vibrios (developed within the human body) typically have infectivity much higher (up to 700-fold) than their environmental counterparts [27, 42]. Typically, due to the contacts between the hosts and the contaminated water or food, vibrios from the environment are ingested into the human body. Through a series of biological, chemical, and genetic interactions during the passage of the bacteria through the human gastrointestinal tract, the environmental vibrios are transferred to human vibrios with much higher infectivity/toxicity that could directly lead to human cholera symptoms [13,21], among which profuse diarrhea and massive fluid loss are most common.

A challenge in the design of effective prevention and intervention strategies for cholera (perhaps also for many other infectious diseases) is the highly heterogeneous pattern in the host response, individual symptoms, and transmission of the disease. These are closely related to the distinct health conditions among different human individuals. For example, some people may not easily become infected with cholera due to the strong immune system inside their bodies or the cholera vaccines they previously received, whereas young children, old people, and those with poor health are much more vulnerable to cholera and likely exhibit severe infections. A comprehensive description of the within-host cholera dynamics that covers all details of the pathogen evolution and transformation inside the human body, while including the individual distinctions across

a large host population, would lead to highly complicated dynamical systems that are challenging to analyze or compute. Alternatively, a popular approach in disease modeling is to utilize the agent-based modeling and simulation technique, where multiple agents reside in networks and interact with each other according to a set of heuristic rules, with an aim of creating or predicting the complex overall system behavior [6, 43]. Advantages of the agent-based modeling include high flexibility and natural incorporation of heterogeneity [45, 48]. However, the nature of the agent-based framework makes it mathematically intractable, and the only way to implement/analyze such a model is through numerical simulation. The overall computational efforts can become prohibitively expensive when the number of interacting agents is large.

Accordingly, we will propose a novel deterministic modeling framework to connect the between-host and within-host dynamics of cholera while keeping the model mathematically and computationally manageable. On the population level, we utilize a Susceptible-Infected-Recovered-Bacteria (SIR-B) model to describe the disease transmission and the interaction between human hosts and environmental pathogens. On the individual host level, we treat each individual as a separate compartment represented by an equation that describes the evolution from environmental vibrios to human vibrios within the human body. Within each individual host, our modeling approach is coarse-grained as the dynamics are described by a single equation characterizing the essential pathogen development from a lower infectious state to a hyper-infectious state. However, since each host is separately modeled, distinctions among different individuals can be naturally incorporated to reflect the heterogeneity of the within-host dynamics. Our primary goal is to conduct a thorough mathematical analysis on the equilibria and their local and global dynamics, then use the simulation results to verify the analytical predictions.

In normal situations, cholera is relatively easy to treat. Oral rehydration therapy using clear water and a modest amount of salt and sugar has saved millions of lives and has reduced overall case fatality rates below 1% [66, 68]. Antibiotics are used to treat severe infections, while their effects in mass administration are unclear as they contribute to increasing antimicrobial resistance [66]. In addition, cholera vaccines, especially the

recently introduced two-dose oral vaccine that is less expensive and more convenient to deliver than its predecessor [46, 64], have been effective in both the prevention and intervention of disease outbreaks. For many developing countries, however, the availability of medical resources significantly limits the implementation of these control measures. Antibiotics, vaccines, and other medicine may be not available or in severe shortage compared to the demands. There may not even be sufficient clean drinking water, salt, and sugar for the basic rehydration practice [4, 15, 38, 39]. Due to the inadequate medical resources, the infection may rapidly spread, leading to unusually high prevalence and attack rates. The risk of transmitting cholera from the environment as well as among human hosts could be significantly increased. Meanwhile, as a result of insufficient medical treatment and sanitation and as feedback of increased infection levels, human contribution (e.g., through shedding) to the environmental pathogen could also increase. These factors worsen and elongate the cholera epidemics.

An important factor in the cholera epidemics and endemics in developing countries is that the medical resources are insufficient to meet the needs of fighting the cholera outbreaks. Indeed, one of the common characteristics among the recent, large-scale cholera outbreaks, including those from Zimbabwe, Haiti, and Yemen, is the difficulty in providing an adequate medical response due to shortages in health professionals and medical supplies [11, 28, 38, 40, 54]. Consequently, a massive surge of cases occurred in these outbreaks, underscoring the importance of medical resources in shaping the cholera epidemics. Thus, we at last focus on investigating how the availability of medical resources would impact the cholera transmission and shape the pattern of a cholera epidemic. To that end, we formulate a system of differential equations to describe cholera transmission dynamics, using a compartmental modeling approach. In addition to the typical compartments involved in cholera models (i.e., the susceptible hosts, the infected/infectious hosts, the recovered hosts, and the pathogen), we introduce another compartment to represent the strength, or availability level, of the medical resources. Our model will then describe the interaction among the hosts, the pathogen, and the medical resources, incorporating both direct and indirect transmission pathways. Particularly, several model

parameters, including the direct and indirect transmission rates and the host shedding rate will explicitly depend on medical resources. As an application of this model, we study the Yemen cholera outbreak during the period of April 2017 to May 2018. Yemen has experienced years of heavy conflicts and wars, severely disrupting society and the public health infrastructure. In particular, 55% of the health facilities in Yemen are no longer fully functional [69]. In October 2016, a small cholera epidemic started in Yemen which, by March 2017, was apparently in decline. However, the outbreak resurged on April 27, 2017, and remained on-going since then, leading to the largest documented cholera epidemic of modern times. By the end of 2017, cumulative cases exceeded 1 million, and by May 2018, more than 1.1 million cases were reported [70]. We conduct data fitting of our model by using the weekly epidemiological reports published by the World Health Organization (WHO) [71]. We particularly emphasize the role of limited medical resources in shaping the Yemen cholera outbreak, by examining the data fitting results at both the national and governorate levels. Our findings contribute to a deeper understanding of the transmission dynamics underlying the Yemen cholera outbreak and provide useful guidelines for the design of future prevention and intervention strategies.

We organize the remainder of this dissertation as follows. In Chapter 2, we describe and analyze the impact of the intrinsic growth of cholera bacteria on the dynamics of cholera. In Chapter 3, we introduce a multi-scale modeling framework. In Chapter 4, we take a practical case to investigate the impact of available medical resources on cholera transmission. Finally, we briefly summarize our work in Chapter 5.

CHAPTER 2

INTRINSIC GROWTH OF BACTERIA IN CHOLERA DYNAMICS

2.1 Logistic growth

We consider the following equations that describe the transmission dynamics of cholera infection by incorporating both direct (i.e., human-to-human) and indirect (i.e., environment-to-human) transmission pathways, each represented by a bilinear incidence. Our focus is on the intrinsic dynamics of the cholera bacteria in this process, represented by the logistic growth model.

$$\begin{aligned}
\frac{dS}{dt} &= \mu N - (\alpha I + \beta B)S - \mu S, \\
\frac{dI}{dt} &= (\alpha I + \beta B)S - \mu I - \delta I, \\
\frac{dR}{dt} &= \delta I - \mu R, \\
\frac{dB}{dt} &= rB\left(1 - \frac{B}{k}\right) - \tau B + \xi I.
\end{aligned} \tag{2.1.1}$$

The parameter $N = S + I + R$ is the total population size of the host individuals with a constant birth and death rate μ. The variables S, I, and R represent the susceptible, infected and recovered individuals, respectively, whereas B represents the concentration of the bacteria in the contaminated water. The prameters α and β denote the direct and indirect transmission rates, respectively, δ is the recovery rate, r is the bacterial intrinsic growth rate, k is the carrying capacity, τ is the bacteria remove rate, and ξ is the rate of contribution from an infected individual to the bacteria population in the environment (e.g., through shedding). We neglect the disease related mortality here. All these parameters are assumed to be possitive.

It can be easily verified that the domain of biological interest

$$\Gamma = \{(S, I, R, B) \in \mathbb{R}^4_+ : \ S + I + R = N\}$$

is positively invariant and attracting with respect to model (2.1.1).

Apparently, there is a unique disease free equilibrium (DFE) at $X_0 = (N, 0, 0, 0)$. We proceed to determine the basic reproduction number $\mathcal{R}_0$ for this model. The compartments I and B are directly related to the disease. Using the notions provided in [55], the non-negative matrix F that denotes the generation of new infections and the non-singular matrix V that denotes the transfer among infectious compartments, are respectively given by

$$F = \begin{bmatrix} \alpha N & \beta N \\ \xi & r \end{bmatrix} \quad \text{and} \quad V = \begin{bmatrix} \mu + \delta & \\ & \tau \end{bmatrix}, \tag{2.1.2}$$

which then lead to the next-generation matrix

$$FV^{-1} = \begin{bmatrix} \frac{\alpha N}{\mu+\delta} & \frac{\beta N}{\tau} \\ \frac{\xi}{\mu+\delta} & \frac{r}{\tau} \end{bmatrix}. \tag{2.1.3}$$

It follows from (2.1.3) that the reproductive number can be represented by

$$\mathcal{R}_0 = \rho(FV^{-1}) = \frac{1}{2}\left(\frac{\alpha N}{\mu+\delta} + \frac{r}{\tau} + \sqrt{\left(\frac{\alpha N}{\mu+\delta} - \frac{r}{\tau}\right)^2 + \frac{4\xi\beta N}{\tau(\mu+\delta)}}\right), \tag{2.1.4}$$

where ρ denotes the spectral radius.

We comment here that the expression for the basic reproduction number is not unique [8,55]. For example, in the above we derived $\mathcal{R}_0$ by treating the intrinsic bacterial growth and host shedding as generation of new infections in B. If, instead, we treat these as transfer of infections and put them in the matrix V, then we obtain another basic

reprodution number

$$\widetilde{\mathcal{R}_0} = \frac{\alpha N}{\mu + \delta} + \frac{\xi \beta N}{(\mu + \delta)(\tau - r)}, \tag{2.1.5}$$

where we assume $\tau \neq r$. Through simple algebraic manipulation, we can show that

$$\mathcal{R}_0 - 1 = \frac{2\left(1 - \frac{r}{\tau}\right)(\widetilde{\mathcal{R}_0} - 1)}{\sqrt{(\frac{\alpha N}{\mu+\delta} - \frac{r}{\tau})^2 + \frac{4\xi\beta N}{\tau(\mu+\delta)}} + 2 - \frac{\alpha N}{\mu+\delta} - \frac{r}{\tau}}.$$

That is, $\mathcal{R}_0 > (respectively, =, <) 1$ if and only if $\widetilde{\mathcal{R}_0} > (=, <) 1$, namely, the two reproduction numbers are equivalent in characterizing disease risks.

2.1.1 Nontrivial equilibria

A nontrivial equilibrium $X = (S, I, R, B)$ for system (2.1.1) satisfies

$$\mu N = (\alpha I + \beta B)S + \mu S, \tag{2.1.6}$$

$$(\alpha I + \beta B)S = (\mu + \delta)I, \tag{2.1.7}$$

$$\delta I = \mu R, \tag{2.1.8}$$

$$\xi I = \frac{r}{k} B^2 + (\tau - r)B. \tag{2.1.9}$$

Letting $\theta = \frac{\mu N}{\mu+\delta}$ and canceling S from (2.1.6) and (2.1.7), we obtain

$$\alpha I^2 + (\mu + \beta B - \alpha\theta)I - \beta\theta B = 0. \tag{2.1.10}$$

Since I is nonnegative, we have $I = g(B)$, where

$$g(B) = \frac{\sqrt{(\mu - \alpha\theta + \beta B)^2 + 4\alpha\beta\theta B} - (\mu - \alpha\theta + \beta B)}{2\alpha}, \ B \geq 0. \tag{2.1.11}$$

In addition, we get $B = p(I)$ from (2.1.10), where

$$p(I) = \frac{\mu I}{\beta(\theta - I)} - \frac{\alpha}{\beta} I, \ I \geq 0. \tag{2.1.12}$$

Hence $B = p(g(B)), \ B \geq 0$, and then we have $g'(B) = 1/p'(g(B)) = 1/p'(I)$. Furthermore, $p(I) = B > 0$ implies that

$$\max\left(0, \theta - \frac{\mu}{\alpha}\right) < I < \theta. \tag{2.1.13}$$

From (2.1.9), if we denote

$$I = q(B) = \frac{r}{\xi k} B^2 + \frac{\tau - r}{\xi} B, \tag{2.1.14}$$

then we have the equation

$$g(B) = q(B), \ B > 0. \tag{2.1.15}$$

Let $m = \min(\theta, \frac{\mu}{\alpha})$. Then $0 < \theta - I < m$ from (2.1.13), and $\frac{\mu}{\alpha}\theta \geq m^2$. Hence we have

$$\mu\theta - \alpha(\theta - I)^2 > \mu\theta - \alpha m^2 = \alpha\left(\frac{\mu}{\alpha}\theta - m^2\right) \geq 0. \tag{2.1.16}$$

Thus

$$g'(B) = 1/p'(I) = \frac{\beta(\theta - I)^2}{\mu\theta - \alpha(\theta - I)^2} > 0 \tag{2.1.17}$$

and

$$g''(B) = \frac{-p''(I)}{p'(I)^3} = \frac{-2\mu\theta g'(B)^3}{\beta(\theta - I)^3} < 0. \tag{2.1.18}$$

On the other hand, we have

$$q''(B) = \frac{2r}{\xi k} > 0. \tag{2.1.19}$$

Notice that $g(0) \geq q(0)$ and

$$g'(0) - q'(0) = \frac{\sqrt{\left(\frac{\alpha N}{\mu+\delta} - \frac{r}{\tau}\right)^2 + \frac{4\xi\beta N}{\tau(\mu+\delta)}} + \left(1 - \frac{\alpha N}{\mu+\delta}\right) + \left(1 - \frac{r}{\tau}\right)}{2\left(1 - \frac{\alpha N}{\mu+\delta}\right)\frac{r}{\tau}}(\mathcal{R}_0 - 1) \tag{2.1.20}$$

with

$$\frac{\sqrt{\left(\frac{\alpha N}{\mu+\delta} - \frac{r}{\tau}\right)^2 + \frac{4\xi\beta N}{\tau(\mu+\delta)}} + \left(1 - \frac{\alpha N}{\mu+\delta}\right) + \left(1 - \frac{r}{\tau}\right)}{2} > \max\left(1 - \frac{\alpha N}{\mu+\delta}, 1 - \frac{r}{\tau}\right).$$

Thus, we obtain the results below for equation (2.1.15):

(1) If $g(0) > q(0)$, i.e., $\frac{\alpha N}{\mu+\delta} > 1$, then the solution is unique.

(2) If $g(0) = q(0)$, i.e., $\frac{\alpha N}{\mu+\delta} \leq 1$. By comparing $g'(0)$ with $q'(0)$, we have

(i) If $\frac{\alpha N}{\mu+\delta} = 1$, then $g'(0+) = +\infty > q'(0)$. The solution exists and is unique.

(ii) If $\frac{\alpha N}{\mu+\delta} < 1$, then

(a) if $g'(0) > q'(0)$, i.e., $\mathcal{R}_0 > 1$, we have a unique solution.

(b) otherwise $g'(0) \leq q'(0)$, i.e., $\mathcal{R}_0 \leq 1$, there is no solution.

Since $\mathcal{R}_0 > \max\left(\frac{\alpha N}{\mu+\delta}, \frac{r}{\tau}\right)$ by (2.1.4), we see that $\frac{\alpha N}{\mu+\delta} \geq 1$ implies $\mathcal{R}_0 > 1$. Therefore, the aforementioned cases yield the following result.

Theorem 1. *The model* (2.1.1) *admits a unique equilibrium, the DFE, if* $\mathcal{R}_0 \leq 1$*; it admits two equilibria, the DFE and the endemic equilibrium (EE), if* $\mathcal{R}_0 > 1$.

2.1.2 Stabilities

We will prove the following two theorems that characterize the main dynamical properties of the system (2.1.1).

Theorem 2. *If* $\mathcal{R}_0 \leq 1$*, then the DFE of the system* (2.1.1) *is globally asymptotically stable in* Γ*. If* $\mathcal{R}_0 > 1$*, the DFE is unstable.*

Proof. Let $X = [I,\, B]^T$. One can verify that

$$X' \leq (F - V)X, \tag{2.1.21}$$

where the matrices F and V are given in equation (2.1.2). Take $\mathbf{u} = \left[\frac{\xi}{\tau}, \mathcal{R}_0 - \frac{\alpha N}{\mu+\delta}\right]$. It then follows from the fact $\mathcal{R}_0 = \rho(FV^{-1}) = \rho(V^{-1}F)$ and direct calculation that $\mathbf{u}$ is a left eigenvector associated with the eigenvalue $\mathcal{R}_0$ of matrix $V^{-1}F$; i.e., $\mathbf{u}V^{-1}F = \mathcal{R}_0\mathbf{u}$. Let us consider the Lyapunov function

$$L = \mathbf{u}V^{-1}X. \tag{2.1.22}$$

Differentiating L along the solutions of the model (2.1.1) and noting the positive components of $\mathbf{u}$, we have

$$L' = \mathbf{u}V^{-1}X' \leq \mathbf{u}V^{-1}(F - V)X = (\mathcal{R}_0 - 1)\mathbf{u}X. \tag{2.1.23}$$

We distinguish two cases for discussion.

Case 1: $\mathcal{R}_0 < 1$. The equality $L' = 0$ implies that $\mathbf{u}X = 0$. This leads to $I = B = 0$. Hence, when $\mathcal{R}_0 < 1$, the model (2.1.1) yield $S = N$ and $I = R = B = 0$. Therefore, the invariant set on which $L' = 0$ contains only one point which is the DFE.

Case 2: $\mathcal{R}_0 = 1$. Then $1 > \max\left(\frac{\alpha N}{\mu+\delta}, \frac{r}{\tau}\right)$, thus we have $\mu + \delta - \alpha N > 0$, and $\tau - r > 0$. The equality $L' = 0$ implies that

$$\alpha\xi I(S - N) + (\mu + \delta - \alpha N)\left(\frac{(\tau - r)(S - N)}{N} - \frac{rB}{k}\right)B = 0. \tag{2.1.24}$$

Hence, $S = N$ and $B = 0$ must hold. It then follows that $I = 0$ and $R = 0$. Once again we obtain $L' = 0$ which contains only DFE.

Therefore, in either case, the largest invariant set on which $L' = 0$ consists of the singleton $X_0 = (N,\, 0,\, 0,\, 0)$. By LaSalle's Invariant Principle [34], the DFE is globally asymptotically stable in Γ if $\mathcal{R}_0 \leq 1$.

In contrast, if $\mathcal{R}_0 > 1$, then it follows from the continuity of vector fields that $L' > 0$ in a neighborhood of the DFE in $\mathring{\Gamma}$, where $\mathring{\Gamma}$ is the interior of Γ. Thus the DFE is unstable by the Lyapunov stability theory. ■

Theorem 3. *If $\mathcal{R}_0 > 1$, the endemic equilibrium (EE) of the model (2.1.1) is locally asymptotically stable. Moreover, the EE is globally asymptotically stable in $\mathring{\Gamma}$ if $N \leq \frac{\delta}{2\alpha}$ holds.*

In order to prove the second part of the theorem, i.e., the global asymptotic stability of the EE, we will utilize the geometric approach originally proposed by Li and Muldowney [36], with the main result summarized below.

Theorem 4. *Consider a dynamical system $\frac{dX}{dt} = f(X)$, where $f : D \mapsto \mathbb{R}^n$ is a C^1 function and $D \subset \mathbb{R}^n$ is a simply connected domain. Assume that there exists a compact absorbing set $K \subset D$ and the system has a unique equilibrium point X^* in D. Let Q be a matrix-valued function defined as*

$$Q = P_f P^{-1} + P J^{[2]} P^{-1},$$

where $P(X)$ is a $\binom{n}{2} \times \binom{n}{2}$ matrix-valued C^1 function in D, P_f is the derivative of P (entry-wise) along the direction of f, and $J^{[2]}$ is the second additive compound matrix of the Jacobian $J(X) = Df(X)$. Then X^* is globally asymptotically stable in D if $\bar{q}_2 < 0$, where

$$\bar{q}_2 = \limsup_{t\to\infty} \sup_{X_0 \in K} \frac{1}{t} \int_0^t m(Q(X(s, X_0)))ds. \tag{2.1.25}$$

Note that $m(Q)$ is the Lozinskiĭ measure of Q with respect to a matrix norm, i.e.,

$$m(Q) = \lim_{h\to 0^+} \frac{|\mathbb{I} + hQ| - 1}{h},$$

where $\mathbb{I}$ represents the identity matrix.

Now we are ready to prove Theorem 3.

Proof. Linearizing the model (2.1.1) at the endemic equilibrium $X_1 = (S_1, I_1, R_1, B_1)$, we

obtain the Jacobian matrix

$$J = \begin{bmatrix} -(\alpha I_1 + \beta B_1 + \mu) & -\alpha S_1 & 0 & -\beta S_1 \\ \alpha I_1 + \beta B_1 & \alpha S_1 - (\mu + \delta) & 0 & \beta S_1 \\ 0 & \delta & -\mu & 0 \\ 0 & \xi & 0 & -\frac{r(2B_1 - k)}{k} - \tau \end{bmatrix} \tag{2.1.26}$$

It is easy to verify that the characteristic polynomial of J is

$$\det(\lambda \mathbb{I} - J) = (\lambda + \mu)(\lambda^3 + x\lambda^2 + y\lambda + z), \tag{2.1.27}$$

where

$$\begin{aligned} x &= \frac{\mu N}{S_1} + \frac{\beta B_1 S_1}{I_1} + \frac{rB_1}{k} + \frac{\xi I_1}{B_1}, \\ y &= \frac{\mu N}{S_1}\left(\frac{rB_1}{k} + \frac{\xi I_1}{B_1}\right) + \frac{\beta \mu N B_1}{I_1} + \alpha(\mu + \delta) I_1 + \frac{\beta r S_1 {B_1}^2}{k I_1}, \\ z &= \frac{\beta r \mu N {B_1}^2}{k I_1} + \alpha(\mu + \delta) I_1 \left(\frac{rB_1}{k} + \frac{\xi I_1}{B_1}\right) + \beta \xi (\mu + \delta) I_1. \end{aligned}$$

Obviously, we have $x > 0$, $y > 0$, and $z > 0$. In addition,

$$\begin{aligned} xy &> \left(\frac{\mu N}{S_1} + \frac{rB_1}{k} + \frac{\xi I_1}{B_1}\right)\left(\frac{\beta \mu N B_1}{I_1} + \alpha(\mu + \delta) I_1 + \frac{\beta r S_1 {B_1}^2}{k I_1}\right), \\ &> \frac{\mu N}{S_1} \cdot \frac{\beta r S_1 {B_1}^2}{k I_1} + \left(\frac{rB_1}{k} + \frac{\xi I_1}{B_1}\right)\left(\frac{\beta \mu N B_1}{I_1} + \alpha(\mu + \delta) I_1\right) \\ &> \frac{\beta r \mu N {B_1}^2}{k I_1} + \alpha(\mu + \delta) I_1 \left(\frac{rB_1}{k} + \frac{\xi I_1}{B_1}\right) + \frac{\xi I_1}{B_1} \cdot \frac{\beta \mu N B_1}{I_1}. \\ &> \frac{\beta r \mu N {B_1}^2}{k I_1} + \alpha(\mu + \delta) I_1 \left(\frac{rB_1}{k} + \frac{\xi I_1}{B_1}\right) + \beta \xi (\mu + \delta) I_1. \\ &= z. \end{aligned}$$

It follows from the Routh–Hurwitz criterion that the endemic equilibrium X_1 is locally asymptotically stable.

Next, we apply the geometric approach based on Theorem 4 to prove the global

stability of endemic equilibrium X_1. Denote $d = \frac{r(2B-k)}{k} + \tau$. Then the Jacobian matrix of the system (2.1.1), after dropping the equation for R, is

$$J_1 = \begin{bmatrix} -(\alpha I + \beta B + \mu) & -\alpha S & -\beta S \\ \alpha I + \beta B & \alpha S - (\mu + \delta) & \beta S \\ 0 & \xi & -d \end{bmatrix},$$

and the associated second additive compound matrix is

$$J_1^{[2]} = \begin{bmatrix} \alpha S - (\alpha I + \beta B + 2\mu + \delta) & \beta S & \beta S \\ \xi & -(\alpha I + \beta B + \mu + d) & -\alpha S \\ 0 & \alpha I + \beta B & \alpha S - \mu - \delta - d \end{bmatrix},$$

Define $P = \text{diag}\left[1, \frac{I}{B}, \frac{I}{B}\right]$ and let f denote the vector field of system (2.1.1). Then

$$P_f P^{-1} = \text{diag}\left[0, \frac{\dot{I}}{I} - \frac{\dot{B}}{B}, \frac{\dot{I}}{I} - \frac{\dot{B}}{B}\right]$$

and

$$PJ_1^{[2]}P^{-1} = \begin{bmatrix} \alpha S - (\alpha I + \beta B + 2\mu + \delta) & \beta S\frac{B}{I} & \beta S\frac{B}{I} \\ \frac{I}{B}\xi & -(\alpha I + \beta B + \mu + d) & -\alpha S \\ 0 & \alpha I + \beta B & \alpha S - \mu - \delta - d \end{bmatrix}.$$

The matrix $Q := P_f P^{-1} + PJ_1^{[2]}P^{-1}$ can be written in a block form as

$$Q = \begin{bmatrix} Q_{11} & Q_{12} \\ Q_{21} & Q_{22} \end{bmatrix},$$

where

$$
\begin{aligned}
Q_{11} &= \alpha S - (\alpha I + \beta B + 2\mu + \delta), \\
Q_{12} &= \left[\beta S\frac{B}{I},\, \beta S\frac{B}{I}\right], \\
Q_{21} &= \left[\frac{I}{B}\xi,\, 0\right]^T, \\
Q_{22} &= \begin{bmatrix} -(\alpha I + \beta B + \mu + d) + \frac{\dot{I}}{I} - \frac{\dot{B}}{B} & -\alpha S \\ \alpha I + \beta B & \alpha S - \mu - \delta - d + \frac{\dot{I}}{I} - \frac{\dot{B}}{B} \end{bmatrix}.
\end{aligned}
$$

We now define the vector norm for any $(x_1,\, x_2,\, x_3) \in \mathbb{R}^3$ as

$$|(x_1,\, x_2,\, x_3)| = \max\left(|x_1|,\, |x_2| + |x_3|\right).$$

Let m denote the Lozinskiĭ measure with respect to this norm. By direct calculation, we find that

$$m(Q) = \sup\left(g_1,\, g_2\right)$$

with $g_1 = m_1(Q_{11}) + |Q_{12}|$, $g_2 = |Q_{21}| + m_1(Q_{22})$. where $|Q_{12}|$ and $|Q_{21}|$ are the matrix norms induced by the L_1 norm, and m_1 denotes the Lozinskiĭ measure with respect to L_1 norm. Specifically,

$$
\begin{aligned}
g_1 &= \alpha S - (\alpha I + \beta B + 2\mu + \delta) + \beta S\frac{B}{I}, \\
g_2 &= \frac{\dot{I}}{I} - \mu - \frac{rB}{k} + \sup\left(0, 2\alpha S - \delta\right).
\end{aligned}
$$

Note that $\alpha S + \beta S\frac{B}{I} - \mu - \delta = \frac{\dot{I}}{I}$. Based on the assumption $N \leq \frac{\delta}{2\alpha}$, we have $2\alpha S - \delta - \frac{rB}{k} \leq 0$, and hence

$$
\begin{aligned}
g_1 &= \frac{\dot{I}}{I} - (\alpha I + \beta B + \mu) \leq \frac{\dot{I}}{I} - \mu, \\
g_2 &\leq \frac{\dot{I}}{I} - \mu.
\end{aligned}
$$

Hence $m(Q) \leq \frac{\dot{I}}{I} - \mu$. In view of $0 \leq I(t) \leq N(t)$, if t is large enough, then

$$\frac{\ln(I(t)) - \ln(I(0))}{t} \leq \frac{\mu}{2}$$

and

$$\frac{1}{t}\int_0^t m(Q)ds \leq \frac{1}{t}\int_0^t \left(\frac{\dot{I}}{I} - \mu\right) ds = \frac{\ln(I(t)) - \ln(I(0))}{t} - \mu \leq -\frac{\mu}{2}.$$

Thus, we have

$$\bar{q_2} := \limsup_{t\to\infty} \frac{1}{t}\int_0^t m(Q)ds \leq -\frac{\mu}{2} < 0,$$

which implies that X_1 is globally aysmptotically stable. ■

Hence, Theorems 1-3 describe the essential dynamics of the model (2.1.1) with logistic growth for the bacteria. In particular, the condition $\mathcal{R}_0 = 1$ is a sharp threshold for stability, and a forward transcritical bifurcation takes places at $\mathcal{R}_0 = 1$.

2.2 Growth with Allee effects

Now we proceed to examine the second type of bacterial intrinsic dynamics: growth with Allee effects, and their impact on disease transmission. To that end, we modify the model (2.1.1) by replacing the logistic growth term with a cubic growth term. Other parts of the model remain unchanged. As a result, we obtain the following system

$$\begin{aligned}
\frac{dS}{dt} &= \mu N - (\alpha I + \beta B)S - \mu S,\\
\frac{dI}{dt} &= (\alpha I + \beta B)S - \mu I - \delta I,\\
\frac{dR}{dt} &= \delta I - \mu R,\\
\frac{dB}{dt} &= rB(B-b)\left(1 - \frac{B}{k}\right) + \xi I,
\end{aligned} \tag{2.2.1}$$

where the positive constant b ($b < k$) is referred to as Allee threshold. All other parameters have the same meanings as those in model (2.1.1). Note that a linear bacterial removal, represented by $-brB$, is already incorporated into the cubic growth term. The

unique DFE $X_0 = (N, 0, 0, 0)$ and the invariant domain Γ remains the same.

The next-generation matrices associated with model (2.2.1) are given by

$$F = \begin{bmatrix} \alpha N & \beta N \\ \xi & 0 \end{bmatrix} \quad \text{and} \quad V = \begin{bmatrix} \mu + \delta & \\ & br \end{bmatrix}. \tag{2.2.2}$$

Hence

$$FV^{-1} = \begin{bmatrix} \frac{\alpha N}{\mu+\delta} & \frac{\beta N}{br} \\ \frac{\xi}{\mu+\delta} & 0 \end{bmatrix}. \tag{2.2.3}$$

It follows that the basic reproductive number for model (2.2.1) is

$$\mathcal{R}_0 = \rho(FV^{-1}) = \frac{1}{2}\left(\frac{\alpha N}{\mu+\delta} + \sqrt{\left(\frac{\alpha N}{\mu+\delta}\right)^2 + \frac{4\xi\beta N}{br(\mu+\delta)}}\right). \tag{2.2.4}$$

2.2.1 Endemic equilibria analysis

A nontrivial equilibrium (S, I, R, B) must satisfy the equations

$$\mu N = (\alpha I + \beta B)S + \mu S, \tag{2.2.5}$$

$$(\alpha I + \beta B)S = (\mu + \delta)I, \tag{2.2.6}$$

$$\delta I = \mu R, \tag{2.2.7}$$

$$\xi I = \frac{r}{k}B(B-b)(B-k). \tag{2.2.8}$$

Since $I > 0$ and $b < k$, it suffices to consider $B \in (0, b)\bigcup(k, \infty)$ based on equation (2.2.8).

(i), $B \in (k, \infty)$. Denote $\theta = \frac{\alpha N}{\mu+\delta}$ and cancel S from (2.2.5) and (2.2.6) to obtain

$$\alpha^2 I^2 + \alpha(\mu - \mu\theta + \beta B)I - \mu\beta\theta B = 0. \tag{2.2.9}$$

Since I is nonnegative, we have $I = g(B)$, where

$$g(B) = \frac{\sqrt{(\mu - \mu\theta + \beta B)^2 + 4\mu\beta\theta B} - (\mu - \mu\theta + \beta B)}{2\alpha},\ B > 0. \tag{2.2.10}$$

Meanwhile, we have $B = p(I)$ from (2.2.9), where

$$p(I) = \frac{\alpha I(\alpha I - \mu(\theta - 1))}{\beta(\mu\theta - \alpha I)},\ I > 0. \tag{2.2.11}$$

Hence $B = p(g(B)), B > 0$. Then we have $g'(B) = 1/p'(g(B)) = 1/p'(I)$. In addition, $p(I) = B > 0$ implies that

$$\max\left(0,\ \frac{\mu}{\alpha}(\theta - 1)\right) < I < \frac{\mu}{\alpha}\theta. \tag{2.2.12}$$

Next, we have $I = q(B)$ from (2.2.8), where

$$q(B) = \frac{r}{\xi k}B(B - b)(B - k). \tag{2.2.13}$$

Thus, any endemic equilibria is determined by the solution of the equation

$$g(B) = q(B),\ B > 0. \tag{2.2.14}$$

Let $m = \mu\min(\theta, 1)$. Then $0 < \mu\theta - \alpha I < m$ from (2.2.12), and $\mu^2\theta \geq m^2$. Hence we have

$$\mu^2\theta - (\mu\theta - \alpha I)^2 > \mu^2\theta - m^2 \geq 0. \tag{2.2.15}$$

Thus

$$g'(B) = 1/p'(I) = \frac{\beta(\mu\theta - \alpha g(B))^2}{\alpha(\mu^2\theta - (\mu\theta - \alpha g(B))^2)} > 0 \tag{2.2.16}$$

and

$$g''(B) = \frac{-p''(I)}{p'(I)^3} = \frac{-2\mu^2\alpha^2\theta g'(B)^3}{\beta(\mu\theta - \alpha g(B))^3} < 0. \tag{2.2.17}$$

On the other hand,

$$q''(B) = \frac{2r}{\xi k}(3B - b - k) > 0 \text{ for } B > k. \tag{2.2.18}$$

Therefore, from the monotonicity and concavity of the curves $I = g(B), B > k$, and $I = q(B), B > k$, we see that (2.2.14) has a unique solution for $B \in (k, \infty)$ since $g(k) > q(k)$.

(ii) $B \in (0, b)$. Set $T(B) = q(B) - g(B)$. Then any positive root of $T(B)$ corresponds to an endemic equilibrium. We claim that $T(B)$ has a unique root in $(0, b)$ if $\mathcal{R}_0 < 1$, either 0 or 1 root in $(0, b)$ if $\mathcal{R}_0 = 1$, and $T(B)$ has 0, 1, or 2 roots in $(0, b)$ if $\mathcal{R}_0 > 1$.

(a) If $\mathcal{R}_0 < 1$, then $\theta < \mathcal{R}_0 < 1$ by (2.2.4). Hence $T(0) = 0, T(b) = -g(b) < 0$, and

$$\begin{aligned}
T'(B) &= \frac{r}{\xi k}(3B^2 - 2(b+k)B + bk) - \frac{\beta(\mu\theta - \alpha g(B))^2}{\alpha(\mu^2\theta - (\mu\theta - \alpha g(B))^2)}, \\
T''(B) &= \frac{2r}{\xi k}(3B - b - k) + \frac{2\mu^2\alpha^2\theta g'(B)^3}{\beta(\mu\theta - \alpha g(B))^3}, \\
T'''(B) &= \frac{6r}{\xi k} - \frac{6\mu^2\alpha^3\theta g'(B)^4(\mu^2\theta + (\mu\theta - \alpha g(B))^2)}{\beta(\mu\theta - \alpha g(B))^4(\mu^2\theta - (\mu\theta - \alpha g(B))^2)}.
\end{aligned}$$

Then we have

$$\begin{aligned}
T'(0) &= \frac{br}{\xi} - \frac{\beta\theta}{\alpha(1-\theta)} = \frac{br(1-\mathcal{R}_0)}{2\xi(1-\theta)}\left(\sqrt{\theta^2 + \frac{4\xi\beta N}{br(\mu+\delta)}} + 2 - \theta\right) > 0, \\
T'(b) &= \frac{br}{\xi k}(b-k) - g'(b) < 0.
\end{aligned}$$

Hence $T(B)$ has at least one root in $(0, b)$ as shown in Figure 2.1 and we will prove such a root is unique. One can verify that

$$\begin{aligned}
T^{(4)}(B) &= -g^{(4)}(B) \\
&= \frac{24\alpha^4\mu^2\theta g'(B)^5[(\mu^2\theta + (\mu\theta - \alpha g(B))^2)^2 + \mu^2\theta(\mu\theta - \alpha g(B))^2]}{\beta(\mu\theta - \alpha g(B))^5(\mu^2\theta - (\mu\theta - \alpha g(B))^2)^2} \\
&> 0,
\end{aligned}$$

which shows that $T''(B)$ is convex. Hence $T''(B)$ has at most two zeros. Meanwhile, since $T'(0) > 0$ and $T(b) < 0$, We will show that $T'(B)$ indeed has only one zero in $(0,\ b)$ through the discussion of the following three cases.

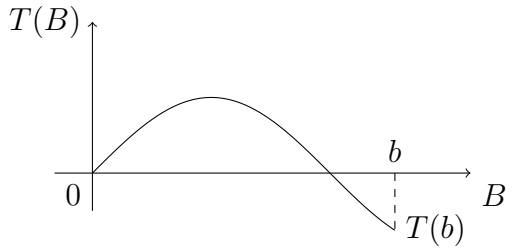

Figure 2.1

An illustration showing the function $T(B)$ has at least one root in $(0,\ b)$

First, suppose that there is no solution in $(0,\ b)$ for $T''(B) = 0$. Then $T'(B)$ is strickly monotone in $(0,\ b)$, $T'(B)$ has at least one zero in $(0,\ b)$, and $T'(B)$ has at most one zero in $(0,\ b)$.

Second, if there exists a unique zero $y \in (0,\ b)$ for $T''(B) = 0$, then $T'(B)$ is strickly monotone in both $(0,\ y)$ and $(y,\ b)$. Thus, $T'(B)$ has at most two zeros, one in $(0,\ y)$ and the otherr in $(y,\ b)$. However, since $T'(0) > 0$ and $T'(b) < 0$, we conclude that there cannot be two zeros in $(0,\ b)$ for $T'(B) = 0$.

Third, assume that $T''(B)$ has two zeros, say $0 < y_1 < y_2 < b$, which leads to $T''(B) > 0$ in $(0,\ y_1)$, $T''(B) < 0$ in $(y_1,\ y_2)$ and $T''(B) > 0$ in $(y_2,\ b)$. Hence, $T'(B)$ is increasing strickly in $(0,\ y_1)$, decreasing strickly in $(y_1,\ y_2)$ and increasing strickly in $(y_2,\ b)$. Thus, $T'(B) = 0$ can only have one root in $(y_1,\ y_2)$.

Consequently, $T'(B)$ has a unique zero in $(0,\ b)$, hence $T(B)$ has no more than two roots in $(0, b)$ since $T(0) = 0$. On the other hand, it is straightforward to observe that $T(B)$ cannot have two roots in $(0,\ b)$ under the conditions we have derived above. Thererfore, we conclude that $T'(B)$ has a unique root in $(0,\ b)$ when $\mathcal{R}_0 < 1$.

(b) If $\mathcal{R}_0 = 1$, then $\theta < 1$, and we have $T(0) = 0, T(b) < 0$ and $T'(0) = 0, T'(b) < 0$. Notice that $T^{(4)}(B) > 0$. We have the following observations.

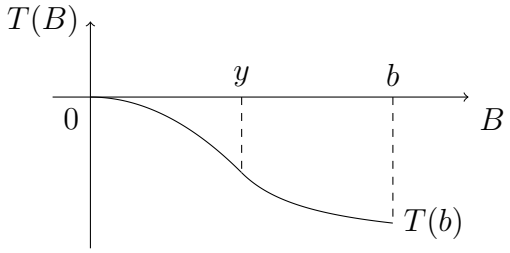

Figure 2.2

An illustration showing the function $T(B)$ is decreasing in $(0,\, b)$

- If $T''(0) \leq 0$, there exists $y > 0$ such that $T''(y) = 0$, and $T''(B) < 0$ in $(0,\, y), T''(B) > 0$ in $(y,\, \infty)$.

  (i) If $y < b$, then $T'(B)$ is strickly decreasing in $(0,\, y)$ and strickly increasing in $(y,\, b)$. Hence $T(B)$ is decreasing from $T(0)$ to $T(b)$, as illustrated in Figure 2.2.

  (ii) If $y \geq b$, then $T'(B)$ is strickly decreasing in $(0,\, b)$, and we obtain that $T'(B) < T'(0) = 0$ in $(0,\, b)$. Hence $T(B) < 0$ in $(0,\, b)$.

  Therefore, $T(B)$ has no zero in $(0,\, b)$ when $T''(0) \leq 0$.

- If $T''(0) > 0$, we prove below that $T(B)$ has a unique zero in $(0,\, b)$.

  (i) If $T''(B)$ has no zero in $(0,\, b)$, then $T''(B) > 0$ in $(0,\, b)$, and then $T'(B)$ is increasing in $(0,\, b)$. But this is impossible since $T'(b) < T'(0)$.

  (ii) If $T''(B)$ has one zero $y \in (0,\, b)$, then $T(B)$ must be convex in $(0,\, y)$ and concave in $(y,\, b)$. Since $T(y) > T(0) = 0$, $T(B)$ has exactly one zero in $(y,\, b)$. See Figure 2.3.

  (iii) If $T''(B)$ has two zero in $(0,\, b)$, then this coincides with the third case discussed before when $\mathcal{R}_0 < 1$, hence $T(B)$ must have a unique zero in $(0,\, b)$.

(c) If $\mathcal{R}_0 > 1$, then $T(B) = q(B) - g(B)$ generally can have 0, 1, or 2 zeros in $(0,\, b)$. It is, however, extremely complicated to algebraically characterize these situations.

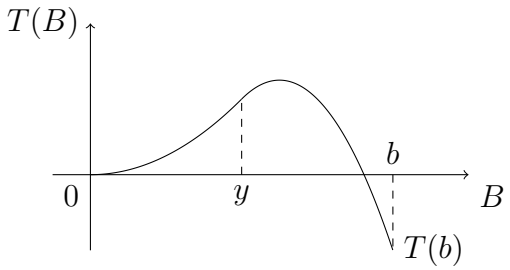

Figure 2.3

An illustration showing the function $T(B)$ has exactly one root in $(y,\, b)$

Instead, we have chosen to graphically illustrate these scenarios in Figure 2.4 which provides a much more intuitive means to observe the three different cases.

In Figure 2.4, we fix all the model parameters except the intrinsic growth rate r, which is allowed to vary. Specifically, $N = 2500,000, \mu = 1/43.5$ per year, $\delta = 1/30$ per day, $\xi = 500$ cells/ml per person per day, $\alpha = 1.48 \times 10^{-8}, \beta = 1.7 \times 10^{-8}, b = 1000$ cells/ml, and $k = 2000$ cells/ml. Obviously, the function $q(B)$ increases with r. On the other hand, the function $g(B)$ does not depend on r and thus remains unchanged when r varies. The results show that when the value of r is low, the curve of $q(B)$ is below that of $q(B)$ and there is no intersection between the two (see Figure 2.4-a). When r is increased to some point, however, the two curves become tangent to each other and there is a unique intersection between the two (see Figure 2.4-b). When r is further increased, there are two intersections between the two curves (see Figure 2.4-c). We summarize the results on the roots of $T(B)$ as follows:

(1) If $\mathcal{R}_0 < 1$, then $T(B)$ has a unique root in $(0, b)$.

(2) If $\mathcal{R}_0 = 1$, then $T(B)$ has either 0 or 1 root in $(0, b)$.

(3) If $\mathcal{R}_0 > 1$, then $T(B)$ can have 0, 1, or 2 roots in $(0, b)$.

To conclude our analysis in this section so far, we state the following theorem.

Theorem 5. *When $\mathcal{R}_0 < 1$, the model (2.2.1) has one endemic equilibrium associated with $B \in (k, \infty)$, and has another endemic equilibrium associated with $B \in (0,\, b)$. When*

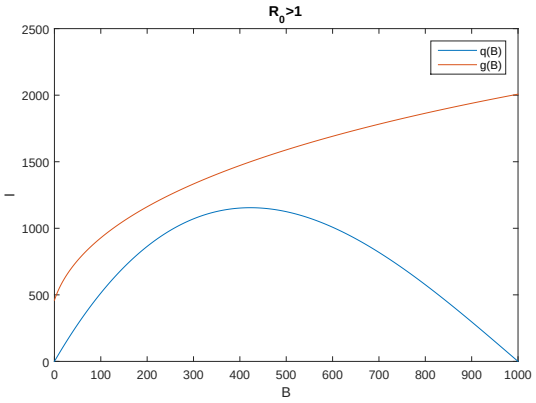

(a) No intersection when $r = 3$

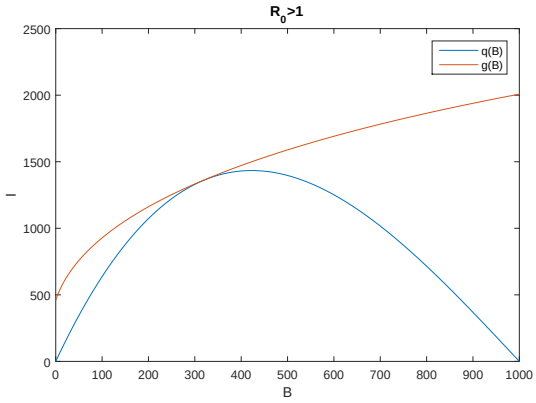

(b) One intersection when $r \approx 3.725$

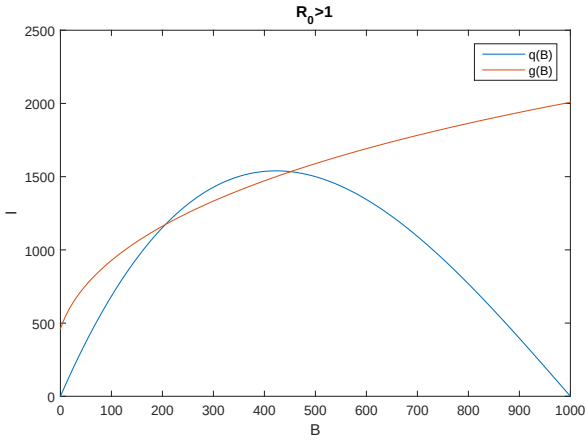

(c) Two intersections when $r = 4$

Figure 2.4

The intersections of $I = q(B)$ and $I = g(B)$ in $(0,\, b)$ when $\mathcal{R}_0 > 1$

$\mathcal{R}_0 = 1$, the model (2.2.1) has one endemic equilibrium with $B \in (k, \infty)$, and has either one or no endemic equilibrium associated with $B \in (0,\, b)$. When $\mathcal{R}_0 > 1$, the model (2.2.1) has one endemic equilibrium with $B \in (k, \infty)$, and can have zero, one, or two endemic equilibria associated with $B \in (0,\, b)$.

In terms of the range of B, Theorem 5 essentially states that when $B \in (k, \infty)$, the model (2.2.1) has a unique endemic equilibrium which always exists; when $B \in (b,\, k)$, the model (2.2.1) has no endemic equilibrium; and when $B \in (0,\, b)$, the model (2.2.1) has a unique endemic equilibrium if $\mathcal{R}_0 < 1$, has either one or no endemic equilibrium if $\mathcal{R}_0 = 1$, and can have zero, one or two endemic equilibria if $\mathcal{R}_0 > 1$.

Additionally, we briefly discuss the scenario when there is a linear bacterial removal

term, independent of the Allee effects, included in the last equation of the model (2.2.1). The equation is now modified as follows:

$$\dot{B}(t) = rB(B-b)\left(1-\frac{B}{k}\right) - \tau B + \xi I, \tag{2.2.19}$$

where $\tau > 0$ denotes the bacterial removal rate. The basic reproductive number of the model now becomes

$$\mathcal{R}_0 = \frac{1}{2}\left(\frac{\alpha N}{\mu+\delta} + \sqrt{\left(\frac{\alpha N}{\mu+\delta}\right)^2 + \frac{4\xi\beta N}{(br+\tau)(\mu+\delta)}}\right). \tag{2.2.20}$$

Meanwhile, equation (2.2.13) becomes

$$I = q(B) = \frac{r}{\xi k}B\left(B^2 - (b+k)B + \frac{k}{r}(br+\tau)\right). \tag{2.2.21}$$

Let us consider the discriminant

$$\Delta = (b+k)^2 - 4\frac{k}{r}(br+\tau) = (b-k)^2 - \frac{4k\tau}{r}.$$

If $\Delta \geq 0$, then there exist $0 < b_1 \leq k_1$ such that

$$q(B) = \frac{r}{\xi k}B(B-b_1)(B-k_1),\ B > 0, \tag{2.2.22}$$

where $b_1 + k_1 = b + k$ and $b_1 k_1 = \frac{k}{r}(br+\tau)$. Note that there is no change to the equation $I = g(B)$ in (2.2.10). Hence, when $\Delta \geq 0$, it is easy to observe that Theorem 5 holds for the modified model, but with b and k replaced by b_1 and k_1, respectively. Basically, it means that when the bacterial removal rate τ is sufficiently small, the dynamical behavior of the system remains the same as that with $\tau = 0$.

On the other hand, when τ is sufficiently large, we have $\Delta < 0$. In this case, with some tedious algebra, it can be shown that the dynamical behavior of the modified system remains the same when $\mathcal{R}_0 \geq 1$, but there are changes of the dynamics in the region

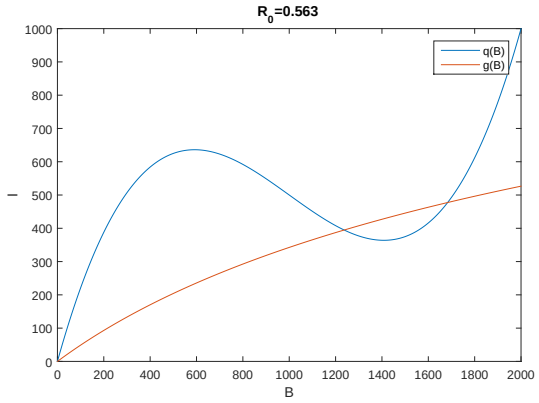

(a) $\tau = 100$

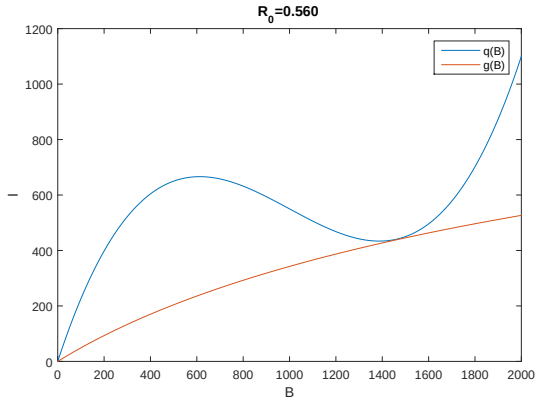

(b) $\tau \approx 285$

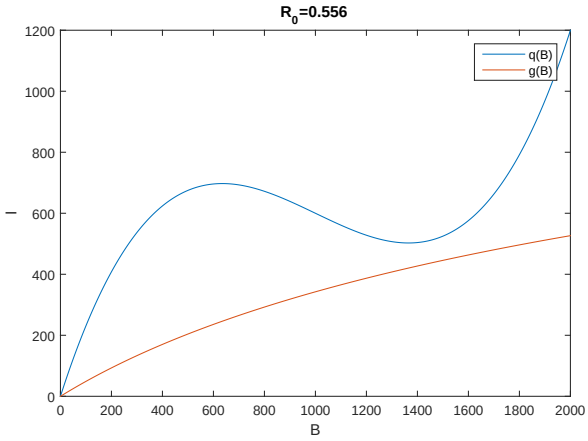

(c) $\tau = 500$

Figure 2.5

The intersections of $I = q(B)$ and $I = g(B)$ in $(0,\, b)$ when $\mathcal{R}_0 < 1$

$0 < \mathcal{R}_0 < 1$. Essentially, now there could be 0, 1, and 2 nontrivial equilibria, represented by the intersections of the two curves $I = q(B)$ and $I = g(B)$, when $\mathcal{R}_0 < 1$, as illustrated in Figure 2.5. An implication is that, at least in part of the region $0 < \mathcal{R}_0 < 1$, it is free of the endemic state and so the disease can be eradicated. This is in contrast to the original model (2.2.1) where there are always two endemic equilibria when $0 < \mathcal{R}_0 < 1$, one with $B \in (k, \infty)$ and the other with $B \in (0,\, b)$ (see Theorem 5). We will provide more numerical results and discuss this difference in next section.

2.2.2 Simulation results and bifurcation diagrams

Due to the complications of the nontrivial equilibria for this model, the stability analysis becomes algebraically intractable. Thus, we have chosen to numerically investigate the stabilities under various scenarios, based on which we are able to sketch the bifurcation diagrams to characterize the main dynamics of model (2.2.1). As shown in the previous section, there is always a unique endemic equilibrium associated with $B \in (k, \infty)$, which we refer to as the upper-branch endemic state. In contrast, the number of endemic equilibria associated with $B \in (0,\, b)$, which we refer to as the lower-branch endemic state, is determined by the value of $\mathcal{R}_0$ as well as other factors.

In Figure 2.6, we plot the time series B vs. t when $T''(0) \leq 0$ for typical scenarios associated with $\mathcal{R}_0 < 1$ (left figure) and $\mathcal{R}_0 > 1$ (right figure), respectively. In each case, we keep $b = 1000$ and $k = 2000$, and we pick an initial value of B in each of the three different ranges for $B : 0 < B < b$, $b < B < k$, and $B > k$. We observe that when $\mathcal{R}_0 < 1$, the orbit starting from $0 < B(0) < b$ (specifically, $B(0) = 500$ here) approaches the DFE at $B = 0$ over time, whereas the other two orbits starting in the regions $b < B(0) < k$ (specifically, $B(0) = 1100$) and $B > k$ (specifically, $B(0) = 3000$) both approach the upper-branch endemic equilibrium, showing a bi-stability pattern. When $\mathcal{R}_0 > 1$ the DFE becomes unstable, and we see that all the three orbits starting with $B(0) > 0$ (specifically, $B(0)$=500, 1500, and 3000 here) approach the upper-branch endemic equilibrium over time, and only the solution starting with $B(0) = 0$ remains at the DFE with $B = 0$.

Meanwhile, in Figure 2.7, we plot the time series B vs. t when $T''(0) > 0$ for typical scenarios associated with different values of $\mathcal{R}_0$. The case with $\mathcal{R}_0 < 1$ is similar to that in Figure 2.6 and thus not shown here. For $\mathcal{R}_0 > 1$, however, our analysis in the previous section predicts the presence of more complex dynamics. Numerically, we find that there exists a critical value of the basic reproductive number, $\mathcal{R}_0^* \approx 2.8$, which distinguishes two different types of solution behaviors, as illustrated in Figure 2.7. When $1 < \mathcal{R}_0 < \mathcal{R}_0^*$, the two orbits starting from $0 < B(0) < b$ ($B(0) = 100$ and

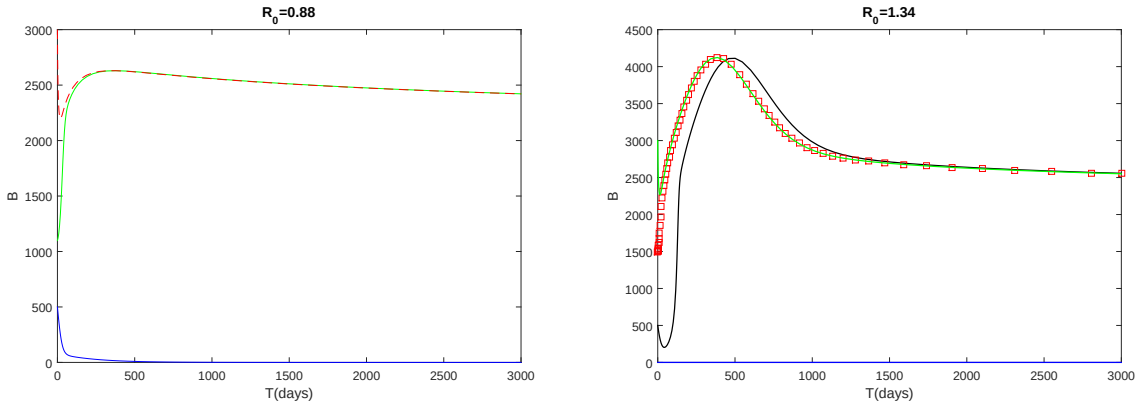

Figure 2.6

Typical solution orbits of B versus time when $T''(0) \leq 0$

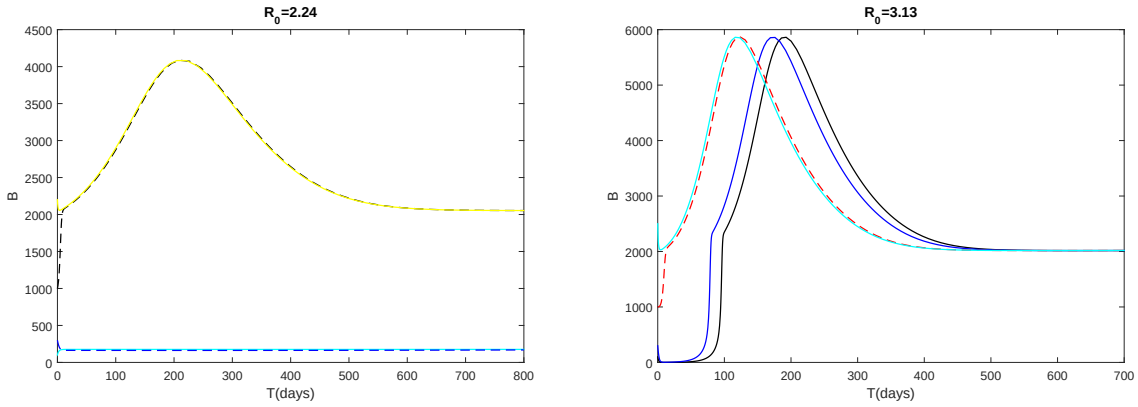

Figure 2.7

Typical solution orbits of B versus time when $T''(0) > 0$

300, respectively) apprach the positive, lower-branch endemic equilibrium, and the other two orbits starting in the regions $b < B(0) < k$ ($B(0)$=1000 and 2200, respectively) approach the upper-branch endemic equilibrium, again showing a bi-stability pattern. When $\mathcal{R}_0 > \mathcal{R}_0^*$, all the four orbits starting with $B(0) > 0$ (specifically, $B(0)$=100, 300, 1000, and 2500 here), including the two very close to the DFE at $B = 0$, approach the upper-branch endemic equilibrium, which is the only stable equilibrium in this scenario.

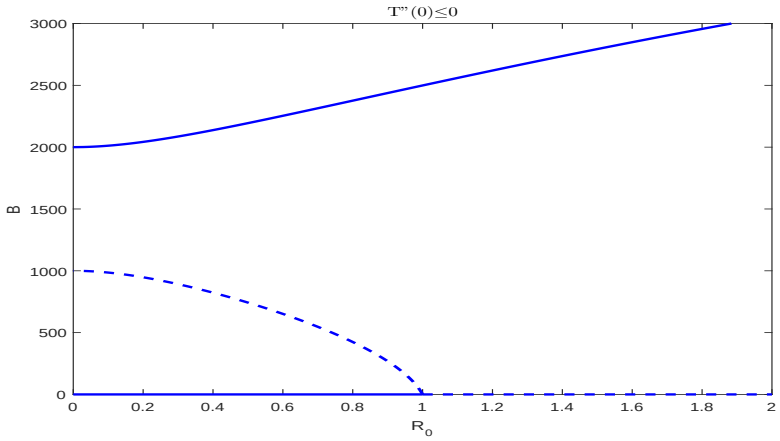

Figure 2.8

A backward bifurcation occurs at $\mathcal{R}_0 = 1$ when $T''(0) \leq 0$

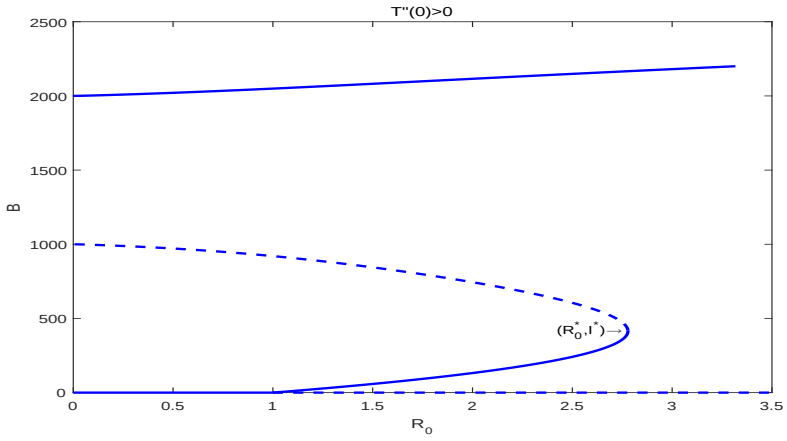

Figure 2.9

A forward hysteresis occurs when $T''(0) > 0$

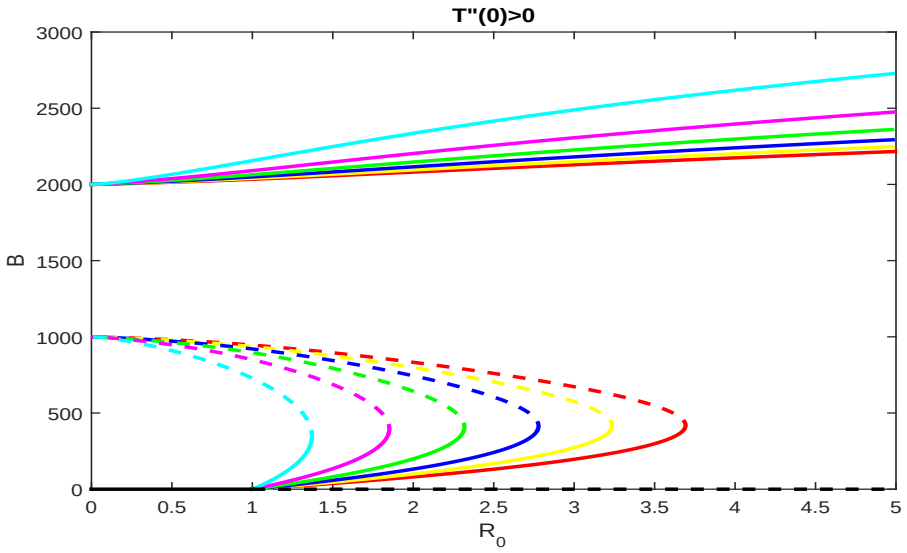

Figure 2.10

Bifurcation diagrams for $T''(0) > 0$ with varied intrinsic growth rate r

We are now ready to sketch the bifurcation diagrams in Figures 2.8 and 2.9. First, we see that as the value of $\mathcal{R}_0$ increases, the solution on the upper-branch equilibrium also increases, which can be reasonably expected. What is more interesting, however, is the solution behavior on the lower-branch equilibrium. Figure 2.8 shows that the lower-branch endemic equilibrium only exists (and is unique) for $\mathcal{R}_0 < 1$. At $\mathcal{R}_0 = 1$, the lower-branch endemic equilibrium intersects the disease-free equilibrium $B = 0$, and a backward transcritical bifurcation [25] takes palce. Solid lines represent stable equilibria and dashed lines represent unstable equilibria. Here $b = 1000$ and $k = 2000$. Figure 2.9, on the other hand, shows that there can be zero, one, or two lower-branch endemic equilibria when $\mathcal{R}_0 \geq 1$, referred to as the forward hysteresis [26]. Specifically, there exists a point $\mathcal{R}_0^* > 1$ such that a turning point bifurcation occurs at $\mathcal{R}_0 = \mathcal{R}_0^*$ and $B = B^*$. When $1 \leq \mathcal{R}_0 < \mathcal{R}_0^*$, there are two lower-brach endemic equilibria; when $\mathcal{R}_0 = \mathcal{R}_0^*$, there is only one such equilibrium; and when $\mathcal{R}_0 > \mathcal{R}_0^*$, there is no such equilibrium. Biologically, these findings indicate that the disease would persist regardless of the value of $\mathcal{R}_0$ based on model (2.2.1). In particular, when $\mathcal{R}_0$ is sufficiently high, all solutions would converge to the upper-branch endemic state, implying a high level of disease risk and potentially large outbreaks of the infection, in the absence of strong

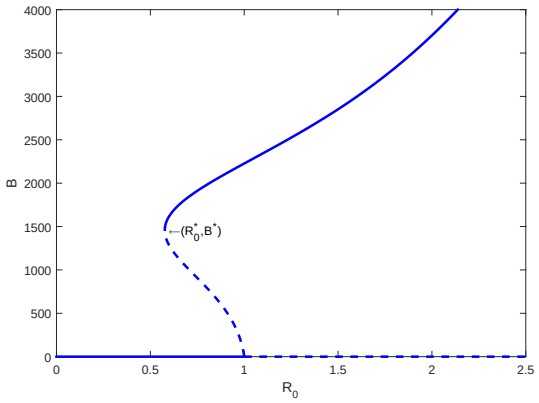

(a) Backward bifurcation, $\tau = 300$

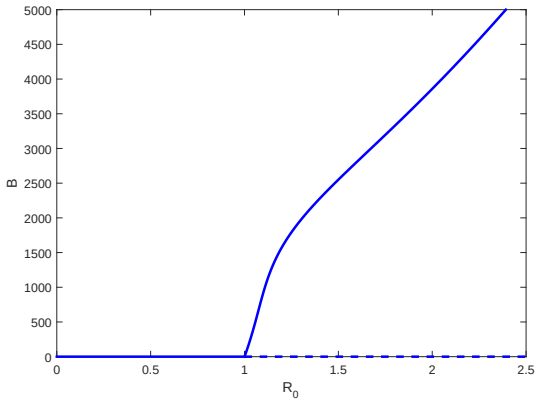

(b) Forward bifurcation, $\tau = 1500$

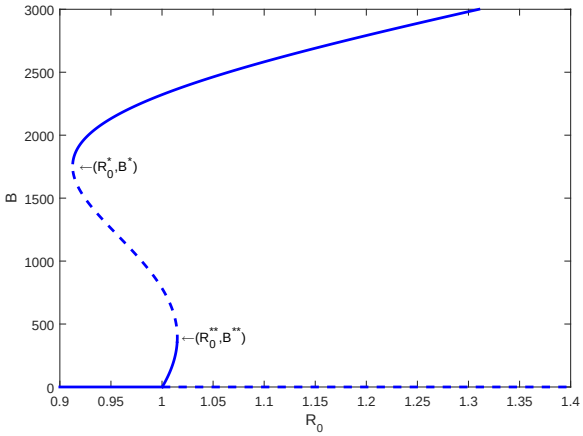

(c) Forward hysteresis and backward bifurcation, $\tau = 800$

Figure 2.11

Typical bifurcation diagrams for the modified model

bacterial removal (represented by $-\tau B$). Additionally, we sketch the forward hysteresis bifurcation diagrams with varied intrinsic growth rate r in Figure 2.10. Results show that as r increases, the regions of the hysteresis are enlarged, whereas the values of the upper-branch endemic equilibrium are reduced.

Finally, we present some results for the modified model; i.e., when the last equation of the model (2.2.1) is replaced by equation (2.2.19). As mentioned before, when the bacterial removal rate τ is small, there is no essential change of the dynamics, thus not discussed here. When τ is large, three typical scenarios are presented in Figure 2.11. For the original model (2.2.1), as can be seen from either Figure 2.8 or 2.9, part of the nontrivial equilibrium solution (on both the upper and lower branches) extends to the

negative quadrant where $\mathcal{R}_0 < 0$ (not shown in the figure). For the modified model, howevere, the presence of a large and positive τ essentially pushes the solution part originally in the negative quadrant, to the positive quadrant with $\mathcal{R}_0 > 0$ (compare to Figures 2.8 and 2.9). As shown in Figure 2.11 (a), when $\tau = 300$, a backward bifurcation takes place at $\mathcal{R}_0 = 1$, and the upper and lower branches of the endemic euqilibria come together and annihilate each other at the turning point ($\mathcal{R}_0^*$, B^*). Connsequently, there could be 0, 1, or 2 endemic equilibria in the region $0 < \mathcal{R}_0 < 1$. As τ is increased, the equilibrium solution is further pushed to the right. Figure 2.11 (c) shows that when $\tau = 800$, a forward hysteresis occurs for $\mathcal{R}_0 > 1$, together with a backward bifurcation for $0 < \mathcal{R}_0 < 1$. The two turning points (for the forward hysteresis and backward bifurcation) both appear in the positive quadrant with $\mathcal{R}_0 > 0$. As τ continues increasing, (e.g., when $\tau = 1500$), the endemic equilibrium solution is completely pushed to the domain $\mathcal{R}_0 > 1$, and a forward bifurcation takes place at $\mathcal{R}_0 = 1$ (see Figure 2.11 (b)) so that the system would exhibit regular threshold dynamics. An important observation is that when the bacterial removal rate τ is large, the disease can be controlled by reducing $\mathcal{R}_0$ to a level lower than $\mathcal{R}_0^*$, where there is no endemic state. This result is distinct from the oringinal model (2.2.1) where $\tau = 0$. In particular, if the value of τ is extremely high (e.g., $\tau = 1500$) such that a forward bifurcation appears, reducing $\mathcal{R}_0$ below unity would be sufficient to eradicate the disease.

2.3 Discussion

A particular challenge in the study of cholera infection is to understand the dynamics of bacteria under various ecological conditions and host settings, which often plays a critical role in shaping the epidemic and endemic patterns. Our focus is to mathematically investigate the intrinsic dynamics of bacterial pathogens and their effects on the transmission and spread of cholera infection. We have employed an SIR-B compartmental model based on differential equations in this study and have carefully investigated two types of nontrivial, nonlinear bacterial dynamics: the logistic growth and the Allee

effects.

The model with logistic growth of bacteria, though more complex than previously studied linear growth models, still exhibits regular threshold dynamics. Specifically, we have shown that when $\mathcal{R}_0 < 1$, the DFE is globally asymptotically stable and the disease would die out; when $\mathcal{R}_0 > 1$, there exists a unique endemic equilibrium which is globally asymptotically stable under appropriate conditions, indicating the persistence of the infection. Hence, the condition $\mathcal{R}_0 = 1$ serves as a sharp threshold for distinguishing disease extinction and persistence. In contrast, the cubic growth model with Allee effects exhibits very rich and complex dynamics. In particular, we find that there are multiple positive endemic states for the model (2.2.1), and the disease can persist in any regime with positive $\mathcal{R}_0$, particularly for $0 < \mathcal{R}_0 < 1$. These observations imply that in the presence of Allee effects among pathogen population, but without strong bacterial removal (that is, independent of Allee effects), there could be some challenges in the control of cholera disease. This could possibly (and partially) explain the persistence of cholera, in several countries/regions in Africa and South Asia. On the other hand, strategic disease prevention and intervention are certainly necessary, as these control efforts can possibly push the infection trajectory from the attraction region of the upper-branch equilibrium to the basins of attraction corresponding to the lower-branch equilibrium and/or the DFE, thus reducing the risk of the disease.

Meanwhile, we have also considered the modified Allee growth model where there is a strong bacterial removal ($-\tau B$) that is independent of Allee effects. We find that when the value of τ is very high; i.e., when the bacterial removal is dominant, the disease can be effectively eradicated by reducing $\mathcal{R}_0$ below unity. Thus, an observation is that water sanitation could play a key role in the control of cholera infection, by strengthening the bacterial removal (i.e., increasing the value of τ) so that the disease could be contained and controlled in the region $0 < \mathcal{R}_0 < 1$ or at least part of it.

In the model (2.2.1), where Allee effects are dominant, due to the interaction between the intrinsic dynamics of pathogens and the external contribution from the infected hosts (e.g., through shedding), the positive equilibria of the bacterial density occur

at two regions: $B > k$ (the upper-branch equilibrium), and $0 < B < b$ (the lower-branch equilibrium) where the microbial population would have declined in the absence of host contribution. The existence and stability of the upper-branch equilibrium imply a potential high risk of infection from bacteria if there is no additional strong bacterial removal. Particularly, our results show that in part of the domain where $\mathcal{R}_0 > 1$, solution orbits starting with low levels of infection would approach the upper-branch equilibrium over time, including a potentially catastrophic occurrence of disease epidemics. Several sudden and extremely severe cholera outbreaks over the last decade (such as those in Zimbabwe, 2008, and in Haiti, 2010) could be possibly linked with this analytical observation. The appearance of the lower-branch equilibria is due to the contribution of fresh bacteria to the aquatic environment by the infected hosts, and this continuous refueling of bacteria overcomes the negative growth of the bacteria within their intrinsic dynamical regime. As a result, endemic states could occur that lead to potential disease outbreaks even when the bacteria population density is low if Allee-independent bacterial removal is absent or is weak.

CHAPTER 3

MULTI-SCALE CHOLERA MODEL

3.1 Model formulation

The between-host dynamics are described by the following SIR model:

$$\begin{aligned} \frac{dS}{dt} =& \mu N - \beta_H SI - \beta_L SB - \mu S, \\ \frac{dI}{dt} =& \beta_H SI + \beta_L SB - (\gamma + \mu) I, \\ \frac{dR}{dt} =& \gamma I - \mu R, \end{aligned} \tag{3.1.1}$$

where B is the concentration of the bacteria *Vibrio cholerae* in the contaminated water. We assume that the natural birth and death rates for human hosts are the same and denoted by μ. Meanwhile, we denote the human-to-human and environment-to-human transmission rates by β_H and β_L, respectively. In addition, γ denotes the recovery rate from the infection. The total population, $N = S + I + R$, remains a constant in this model, and thus, we may drop the equation for R in the analysis of the model.

To emphasize the distinctions among human individuals in the within-host dynamics, we formulate an equation for each individual host:

$$\frac{dZ_i}{dt} = c_i B - \xi_i Z_i, \qquad i = 1, 2, \cdots, N. \tag{3.1.2}$$

Here Z_i represents the concentration of human vibrios within the body of the ith individual, $i = 1, 2, \cdots, N$. The environmental vibrios that are ingested into the human body are transferred, at a rate c_i, to human vibrios which typically have much higher infectivity/toxicity and could directly lead to human cholera symptoms. Meanwhile, the

human vibrios are removed from the human body at a rate ξ_i due to natural death of the bacteria, shedding of the bacteria to the environment, etc. We assume

$$c_i \geq 0, \quad \xi_i > 0, \qquad i = 1, 2, \cdots, N. \tag{3.1.3}$$

The values of c_i and ξ_i will highlight the distinctions among different human individuals. For example, for individuals who are especially vulnerable to cholera (such as young children, old people, or those with poor health), the rate c_i will be relatively high. In contrast, for individuals who are immune to cholera (due to vaccination, recovery from cholera, etc.) or otherwise are healthy and have a strong immune system, the rate c_i will be close or equal to 0.

Meanwhile, we assume that for each individual i, a portion p_i of the removed human vibrios are shed out of the human body and transfer back to the environmental virbrios. The following equation thus describes the dynamics of the vibrios in the environment:

$$\frac{dB}{dt} = \alpha B \left(1 - \frac{B}{\kappa}\right) + \sum_{i=1}^{N} p_i \xi_i Z_i - \delta B, \tag{3.1.4}$$

where the intrinsic growth of the bacteria is modeled by a logistic model with the growth rate α and carrying capacity κ. The shedding from each human individual contributes to the growth of the bacterial concentration in the environment. In addition, δ denotes the natural death rate of the bacteria. In addition, we make the following two assumptions:

(A1) At any time t, if $I(t) > 0$, then there exists at least one i such that $Z_i(t) > 0$.

(A2) $\delta - \sum_{i=1}^{N} p_i c_i > 0$.

The condition (A1) sets a positive relationship between the disease prevalence and the within-host dynamics. The condition (A2) implies that in the absence of the intrinsic bacterial growth ($\alpha = 0$), the environmental vibrios would die away eventually.

3.2 Separation of scales

A simplified model analysis can be conducted by separating the time scales, since the within-host dynamics are on a fast scale and typically range from several hours to a few days, whereas the between-host dynamics and environmental bacterial evolution are on a slow scale and normally take place in months and years. Thus, we may treat the slow variable B as a constant in the fast-scale (within-host) model (3.1.4) to obtain

$$Z_i(t) = \frac{c_i B}{\xi_i} + \left(Z_i(0) - \frac{c_i B}{\xi_i} \right) e^{-\xi_i t} . \tag{3.2.1}$$

Note that $\xi_i > 0$. Equation (3.2.1) shows that for each fixed $B > 0$, Z_i would exponentially converge to its equilibrium (i.e., steady state) $c_i B/\xi_i$, $i = 1, 2, \cdots, N$. Hence, we may approximate each fast variable Z_i at its steady state in the slow-scale environmental bacterial equation (3.1.4). As a result, we obtain

$$\frac{dB}{dt} = \left(\sum_{i=1}^{N} p_i c_i + \alpha - \delta \right) B - \frac{\alpha}{\kappa} B^2 . \tag{3.2.2}$$

Equation (3.2.2) is a Bernoulli equation and can be analytically solved to obtain:

$$B(t) = \left(-\frac{d_2}{d_1} + \left(\frac{1}{B(0)} + \frac{d_2}{d_1} \right) e^{-d_1 t} \right)^{-1} \text{ if } d_1 \neq 0, \tag{3.2.3}$$

and

$$B(t) = \left(\frac{1}{B(0)} - d_2 t \right)^{-1} \text{ if } d_1 = 0, \tag{3.2.4}$$

where

$$d_1 = \alpha - \delta + \sum_{i=1}^{N} p_i c_i , \qquad d_2 = -\frac{\alpha}{\kappa} . \tag{3.2.5}$$

It is easy to observe that

(i) if $d_1 \leq 0$, then $B(t) \to 0$ as $t \to \infty$;

(ii) if $d_1 > 0$, then $B(t) \to -d_1/d_2$ as $t \to \infty$.

Next, we will discuss the fully coupled system that consists of equations (3.1.1), (3.1.2) and (3.1.4).

3.3 Basic reproduction number

It is obvious that there is a unique trivial equilibrium, or disease-free equilibrium (DFE), at

$$S = N, \quad I = B = Z_1 = \cdots = Z_N = 0. \tag{3.3.1}$$

We can still use the next-generation matrix technique to compute the basic reproduction number, $\mathcal{R}_0$, for this model. We re-write the equations directly related to the infection as follows:

$$\begin{bmatrix} Z_1' \\ \vdots \\ Z_N' \\ B' \\ I' \end{bmatrix} = \begin{bmatrix} 0 \\ \vdots \\ 0 \\ \alpha B\big(1 - \frac{B}{\kappa}\big) \\ \beta_H SI + \beta_L SB \end{bmatrix} - \begin{bmatrix} \xi_1 Z_1 - c_1 B \\ \vdots \\ \xi_N Z_N - c_N B \\ \delta B - \sum_{i=1}^{N} p_i \xi_i Z_i \\ (\mu + \gamma) I \end{bmatrix},$$

where the first part on the right-hand side represents the generation of new infection, and the second part represents the transfer among the disease compartments. The next-generation matrices are given by

$$F = \begin{bmatrix} 0 & \cdots & 0 & 0 & 0 \\ \vdots & \ddots & \vdots & \vdots & \vdots \\ 0 & \cdots & 0 & 0 & 0 \\ 0 & \cdots & 0 & \alpha & 0 \\ 0 & \cdots & 0 & \beta_L N & \beta_H N \end{bmatrix} =: \begin{bmatrix} O & O \\ O & E \end{bmatrix}$$

and

$$V = \begin{bmatrix} \xi_1 & \cdots & 0 & -c_1 & 0 \\ \vdots & \ddots & \vdots & \vdots & \vdots \\ 0 & \cdots & \xi_N & -c_N & 0 \\ -p_1\xi_1 & \cdots & -p_N\xi_N & \delta & 0 \\ 0 & \cdots & 0 & 0 & \mu+\gamma \end{bmatrix} =: \begin{bmatrix} A & B \\ C & D \end{bmatrix}.$$

The dimensions of these (non-zero) matrix blocks A, B, C, D, and E are $N \times N$, $N \times 2$, $2 \times N$, 2×2, and 2×2, respectively.

The basic reproduction number is then determined by the spectral radius of the matrix FV^{-1}. The inverse of V can be calculated by using the flowing result:

Theorem 6. [5] *Consider any square matrix in the form of* $V = \begin{bmatrix} A & B \\ C & D \end{bmatrix}$ *where* A, B, C *and* D *are matrix blocks, with* A *and* D *being square. Then the matrix* V *is invertible if and only if* A *and* $D - CA^{-1}B$ *are invertible, and*

$$V^{-1} = \begin{bmatrix} A^{-1} + A^{-1}B\big(D - CA^{-1}B\big)^{-1}CA^{-1} & -A^{-1}B\big(D - CA^{-1}B\big)^{-1} \\ -\big(D - CA^{-1}B\big)^{-1}CA^{-1} & \big(D - CA^{-1}B\big)^{-1} \end{bmatrix}. \tag{3.3.2}$$

Note, however, that E is the only non-zero block in our matrix F. Hence, it is clear that

$$\mathcal{R}_0 = \rho\big(FV^{-1}\big) = \rho\Big(E\big(D - CA^{-1}B\big)^{-1}\Big),$$

where

$$E(D - CA^{-1}B)^{-1} = \begin{bmatrix} \alpha & 0 \\ \beta_L N & \beta_H N \end{bmatrix} \cdot \begin{bmatrix} \frac{1}{\delta - \sum_{i=1}^{N} p_i c_i} & 0 \\ 0 & \frac{1}{\mu+\gamma} \end{bmatrix} = \begin{bmatrix} \frac{\alpha}{\delta - \sum_{i=1}^{N} p_i c_i} & 0 \\ \frac{\beta_L N}{\delta - \sum_{i=1}^{N} p_i c_i} & \frac{\beta_H N}{\mu+\gamma} \end{bmatrix}.$$

Note that each component in the matrix above is positive based on the assumption (A2). Therefore, we obtain

$$\mathcal{R}_0 = \max\big(R_1\,,\ R_2\big), \tag{3.3.3}$$

where

$$R_1 = \frac{\alpha}{\delta - \sum_{i=1}^{N} p_i c_i} \text{ and } R_2 = \frac{\beta_H N}{\mu + \gamma}.$$

Theorem 7. *If $\mathcal{R}_0 \leq 1$, the DFE is globally asymptotically stable.*

Proof. Let $\mathbf{y} = (Z_1, Z_2, ..., B, I)^T$. One can verify that

$$\frac{d\mathbf{y}}{dt} \leq (F - V)\mathbf{y}.$$

If $R_1 \neq R_2$, take

$$\mathbf{u} = (0, ..., 0, x_1, x_2),$$

where

$$x_1 = (R_2 - R_1)^2 + (\mathcal{R}_0 - R_1)\left(\frac{\beta_L N}{\mu + \gamma} - (R_2 - R_1)\right),$$

$$x_2 = (\mathcal{R}_0 - R_1)(R_2 - R_1).$$

It then follows from the fact $\mathcal{R}_0 = \rho(FV^{-1}) = \rho(V^{-1}F)$ and direct calculation that $\mathbf{u}$ is a left eigenvector associated with the eigenvalue $\mathcal{R}_0$ of the matrix $V^{-1}F$; i.e., $\mathbf{u}V^{-1}F = \mathcal{R}_0\mathbf{u}$. Let us consider a Lyapunov function $\mathcal{L} = \mathbf{u}V^{-1}\mathbf{y}$ and differentiate $\mathcal{L}$ along the solutions of (3.1.1), (3.1.2) and (3.1.4), we have

$$\mathcal{L}' = \mathbf{u}V^{-1}\mathbf{y}' \leq \mathbf{u}V^{-1}(F - V)\mathbf{y} = (\mathcal{R}_0 - 1)\mathbf{u}\mathbf{y}. \tag{3.3.4}$$

Case 1: $\mathcal{R}_0 < 1$. The equality $\mathcal{L}' = 0$ implies that $\mathbf{u}\mathbf{y} = 0$. This leads to $x_1 B + x_2 I = 0$, which gives us $B = 0, I \geq 0$ by noting that $x_1 > 0, x_2 \geq 0$. If $I > 0$, then equations of (3.1.1) yield $I = \frac{\mu}{\beta_H}(R_2 - 1) < \frac{\mu}{\beta_H}(\mathcal{R}_0 - 1) < 0$. The contradiction shows that $I = 0$, hence $\mathbf{y} = 0$. Therefore, the invariant set on which $\mathcal{L}' = 0$ contains only one point which is the DFE.

Case 2: $\mathcal{R}_0 = 1$. The equality $\mathcal{L}' = 0$ implies that $\mathbf{y}' = (F - V)\mathbf{y}$, which gives us $B = 0$ and $S = N$. Thus, $\mathbf{y} = 0$ again holds.

Therefore, in either case, the largest invariant set on which $\mathcal{L}' = 0$ consists of the

singleton $E_0 = (N, 0, ..., 0)$. By LaSalle's Invariant Principle [34], the DFE is globally asymptotically stable if $\mathcal{R}_0 \leq 1$.

If $R_1 = R_2$, it is easily to obtain the same results by fixing $\mathbf{u} = (0, ..., 0, 1, 0)$. ■

3.4 Equilibria analysis

We denote a nontrivial equilibrium by

$$X^* = \big(B^*, S^*, I^*, Z_1^*, Z_2^*, \cdots, Z_N^*\big),$$

where, for convenience of algebraic manipulation, we put B^* as the first component. Hence, we have

$$\begin{aligned}
\mu N - \beta_H S^* I^* - \beta_L S^* B^* - \mu S^* &= 0\,,\\
\beta_H S^* I^* + \beta_L S^* B^* - (\gamma + \mu) I^* &= 0\,,\\
\alpha B^* \left(1 - \frac{B^*}{\kappa}\right) + \sum_{i=1}^{N} p_i \xi_i Z_i^* - \delta B^* &= 0\,,\\
c_i B^* - \xi_i Z_i^* &= 0\,.
\end{aligned} \tag{3.4.1}$$

From the last two equations in (3.4.1) we obtain

$$\left(\left(\sum_{i=1}^{N} p_i c_i + \alpha - \delta\right) - \frac{\alpha}{\kappa} B^*\right) B^* = 0\,. \tag{3.4.2}$$

The solution of equation (3.4.2) is given by $B^* = 0$, or

$$B^* = \frac{\kappa}{\alpha}\left(\sum_{i=1}^{N} p_i c_i + \alpha - \delta\right) = \kappa\left(1 - \frac{1}{R_1}\right),$$

where R_1 is defined in (3.3.3). It is clear to see that $B^* > 0$ if and only if $R_1 > 1$. Also, note that the condition $R_1 > 1$ is equivalent to $d_1 > 0$, and that $\kappa\big(1 - \frac{1}{R_1}\big) = -\frac{d_1}{d_2}$, where d_1 and d_2 are defined in (3.2.5). Hence, the result here is consistent with our findings based on the separation of scales.

When $R_1 \leq 1$, the only non-negative solution for B^* is $B^* = 0$. Consequently, $Z_i^* = 0$ for $1 \leq i \leq N$. Meanwhile, the first two equations in (3.4.1) yield

$$\begin{aligned} \mu N - \beta_H S^* I^* - \mu S^* &= 0\,, \\ \beta_H S^* I^* - (\gamma + \mu) I^* &= 0\,. \end{aligned}$$

In addition to the trivial solution $(I^*, S^*) = (0,\, N)$, there is a unique nontrivial solution given as

$$(I^*, S^*) = \Big(\frac{\mu}{\beta_H}\big(R_2 - 1\big),\ \frac{\gamma + \mu}{\beta_H}\Big), \tag{3.4.3}$$

where R_2 is defined in (3.3.3). Obviously $I^* > 0$ if and only if $R_2 > 1$. In this case we obtain a nontrivial boundary equilibrium.

When $R_1 > 1$, then $B^* > 0$. The last equation in (3.4.1) yields

$$Z_i^* = \frac{c_i B^*}{\xi_i}\,, \qquad i = 1, 2, \cdots, N.$$

Meanwhile, the second equation of (3.4.1) yields

$$S^* = \frac{(\gamma + \mu) I^*}{\beta_H I^* + \beta_L B^*} > 0$$

provided that $I^* > 0$. Adding the first two equations in (3.4.1), we obtain

$$\mu N = \mu S^* + (\mu + \gamma) I^*,$$

which yields

$$S^* = N - \left(1 + \frac{\gamma}{\mu}\right) I^*.$$

Substituting this into the second equation of (3.4.1), we obtain

$$\beta_H \left(1 + \frac{\gamma}{\mu}\right) (I^*)^2 + \left((\gamma + \mu)\left(1 + \frac{\beta_L}{\mu} B^*\right) - \beta_H N\right) I^* - \beta_L B^* N = 0. \tag{3.4.4}$$

Clearly, when $B^* > 0$, there is only one positive root, I^*, for equation (3.4.4). In this case we have a unique endemic equilibrium.

Summarizing the results above, we have the following theorem.

Theorem 8. *The system has a non-trivial, non-negative equilibrium if and only if* $\mathcal{R}_0 > 1$. *Specifically,*

1) If $R_1 \leq 1$ *and* $R_2 > 1$, *then there is a unique boundary equilibrium* X_1^* *represented by* $I^* = \frac{\mu}{\beta_H}\big(R_2 - 1\big)$, $S^* = \frac{\gamma+\mu}{\beta_H}$, *and* $B^* = Z_1^* = \cdots = Z_N^* = 0$.

2) If $R_1 > 1$, *then there is a unique endemic equilibrium* X_2^* *represented by* $B^* = \kappa\big(1 - \frac{1}{R_1}\big)$, $Z_i^* = \frac{c_i B^*}{\xi_i}$ $(1 \leq i \leq N)$, $I^* > 0$, *and* $S^* = \frac{(\gamma+\mu)I^*}{\beta_H I^* + \beta_L B^*}$.

Note that the boundary equilibrium X_1^* means that the between-host dynamics are totally decoupled from the environment and the within-host dynamics; that is, the environmental pathogen concentration and the within-host pathogen load have no impact on the disease prevalence. This is unreasonable for a water-borne disease such as cholera. Indeed, our assumption (A1) excludes the boundary equilibrium X_1^*. Hence, we only need to focus on the endemic equilibrium X_2^*.

The Jacobian at the endemic equilibrium is then given by

$$J(X_2^*) = \begin{bmatrix} \alpha - \delta - \frac{2\alpha}{\kappa}B^* & 0 & 0 & p_1\xi_1 & p_2\xi_2 & \cdots & p_N\xi_N \\ -\beta_L S^* & \theta^* & -\beta_H S^* & 0 & 0 & \cdots & 0 \\ \beta_L S^* & \beta_H I^* + \beta_L B^* & \beta_H S^* - (\gamma+\mu) & 0 & 0 & \cdots & 0 \\ c_1 & 0 & 0 & -\xi_1 & 0 & \cdots & 0 \\ c_2 & 0 & 0 & 0 & -\xi_2 & \cdots & 0 \\ \vdots & \vdots & \vdots & \vdots & \vdots & \ddots & \vdots \\ c_N & 0 & 0 & 0 & 0 & \cdots & -\xi_N \end{bmatrix},$$

where $\theta^* = -(\beta_H I^* + \beta_L B^* + \mu)$. After some algebraic manipulation, the characteristic polynomial associated with $J(X_2^*)$ can be found as

$$\det\big(\lambda\mathbb{I} - J(X_2^*)\big) = \Gamma_1(\lambda)\Gamma_2(\lambda), \tag{3.4.5}$$

where

$$\Gamma_1(\lambda) = \det \begin{bmatrix} \lambda + \beta_H I^* + \beta_L B^* + \mu & \beta_H S^* \\ -\big(\beta_H I^* + \beta_L B^*\big) & \lambda - \beta_H S^* + \gamma + \mu \end{bmatrix}$$

$$= \lambda^2 + \big(\beta_H I^* + \beta_L B^* - \beta_H S^* + \gamma + 2\mu\big)\lambda$$

$$+ (\beta_H I^* + \beta_L B^* + \mu)(\gamma + \mu) - \mu\beta_H S^*$$

and

$$\Gamma_2(\lambda) = \left(\lambda + \delta - \alpha + \frac{2\alpha}{\kappa} B^*\right) H(\lambda) + \sum_{i=1}^{N} p_i \xi_i c_i \frac{H(\lambda)}{\lambda + \xi_i} \tag{3.4.6}$$

with

$$H(\lambda) = (\lambda + \xi_1)(\lambda + \xi_2) \cdots (\lambda + \xi_N).$$

One can easily see that $\beta_H S^* < \gamma + \mu$, and thus each coefficient of $\Gamma_1(\lambda)$ is positive. Consequently, the two roots of $\Gamma_1(\lambda)$ both have negative real parts. Meanwhile, note that when $R_1 > 1$, we have

$$\delta - \alpha + \frac{2\alpha}{\kappa} B^* = 2\sum_{i=1}^{N} p_i c_i + \alpha - \delta > \sum_{i=1}^{N} p_i c_i > 0\,.$$

Thus, each coefficient in the polynomial $\Gamma_2(\lambda)$ is positive.

Theorem 9. *When $R_1 > 1$, the endemic equilibrium X_2^* is locally asymptotically stable.*

Proof. We only need to show that each root of $\Gamma_2(\lambda)$ has a negative real part. Let $\rho > 0$ (to be determined), and let

$$\gamma_\rho = \{z | z = \rho e^{i\theta}, \frac{\pi}{2} \le \theta \le \frac{3\pi}{2}\} \bigcup \{z | z = yi, -\rho \le y \le \rho\}, \text{ where } i^2 = -1,$$

be a simple closed contour. Denote $F(\lambda) = (\lambda + A)H(\lambda)$, where $A = \delta - \alpha + \frac{2\alpha}{\kappa} B^*$, then $\Gamma_2(\lambda) = F(\lambda) + H(\lambda) \sum_{k=1}^{N} \frac{p_k c_k \xi_k}{\lambda + \xi_k}$. Obviously, $\Gamma_2(\lambda)$ and $F(\lambda)$ are both analytic inside and on γ. We will show that

$$|\Gamma_2(\lambda) - F(\lambda)| < |F(\lambda)| \text{ on } \gamma_\rho. \tag{3.4.7}$$

By Rouché's Theorem, $\Gamma_2(\lambda)$ and $F(\lambda)$ have the same number of zeros, counting muli-plicities, inside γ_ρ, which is in the left half complex plane.

(i) If $\lambda = yi, -\rho \le y \le \rho$, then

$$\begin{aligned}|\Gamma_2(yi) - F(yi)| &= \left| H(yi) \sum_{k=1}^{N} \frac{p_k c_k \xi_k}{yi + \xi_k} \right| \le |H(yi)| \sum_{k=1}^{N} \left| \frac{p_k c_k \xi_k}{\sqrt{y^2 + \xi_k^2}} \right| \\ &\le |H(yi)| \sum_{k=1}^{N} p_k c_k < |H(yi)| A \\ &\le |H(yi)||A + yi| = |F(yi)|.\end{aligned}$$

(ii) If $\lambda = \rho e^{i\theta},\ \frac{\pi}{2} \le \theta \le \frac{3\pi}{2},\ \rho > 0$, then

$$|\Gamma_2(\rho e^{i\theta}) - F(\rho e^{i\theta})| = \left| H(\rho e^{i\theta}) \sum_{k=1}^{N} \frac{p_k c_k \xi_k}{\rho e^{i\theta} + \xi_k} \right| \le |H(\rho e^{i\theta})| \sum_{k=1}^{N} \frac{p_k c_k \xi_k}{|\rho e^{i\theta} + \xi_k|}.$$

Notice that $\lim\limits_{\rho\to\infty} \sum\limits_{k=1}^{N} \frac{p_k c_k \xi_k}{|\rho e^{i\theta} + \xi_k|} = 0$ and $\lim\limits_{\rho\to\infty} |\rho e^{i\theta} + A| = +\infty$. Hence we can choose some $\rho > \max\{A, \xi_1, ..., \xi_N\}$ such that $\sum\limits_{k=1}^{N} \frac{p_k c_k \xi_k}{|\rho e^{i\theta} + \xi_k|} < |\rho e^{i\theta} + A|$. Thus, (3.4.7) holds for some ρ. Since all $N+1$ zeros of $F(\lambda)$ are inside γ_ρ, we obtain that all $N+1$ zeros of $\Gamma_2(\lambda)$ are inside γ_ρ, i.e., the real part of every zero of $\Gamma_2(\lambda)$ is negative. Therefore, X_2^* is locally stable. ■

In contrast, the global asymptotic stability of an endemic equilibrium is usually difficult to establish, when the dimension of the system is high. The proof of such global stability, if available, normally comes with additional conditions on the model. In our case, we have the following result.

Theorem 10. *When $R_1 > 1$, the endemic equilibrium X_2^* is globally asymptotically stable if $2 + \frac{B}{B^*} \le \frac{I}{I^*} + \frac{S^*}{S} + \frac{SI^*B}{S^*IB^*}$.*

Proof. We consider a Lyapunov function

$$\mathcal{L} = a_1 D_1 + a_2 D_2 + a_3 D_3 + \sum_{i=1}^{N} A_i E_i,$$

where

$$D_1 = \left(S - S^* - S^* \ln\left(\frac{S}{S^*}\right)\right),\ D_2 = \left(I - I^* - I^* \ln\left(\frac{I}{I^*}\right)\right),$$
$$D_3 = \left(B - B^* - B^* \ln\left(\frac{B}{B^*}\right)\right),\ E_i = \left(Z_i - Z_i^* - Z_i^* \ln\left(\frac{Z_i}{Z_i^*}\right)\right), i = 1, 2, ..., N,$$

and $a_j > 0$ $(j = 1, 2, 3, 4)$, $A_i > 0$ $(i = 1, 2, ..., N)$ are constants to be determined.

It is easy to verify that $\mathcal{L} \geq 0$ for all $S, I, B, Z_i, (i = 1, 2, ..., N) > 0$, and $\mathcal{L} = 0$ if and only if $(S, I, B, Z_1, ...Z_N) = X_2^*$. Differentiating $\mathcal{L}$ along X_2^*, we obtain

$$\begin{aligned}
\mathcal{L}' &= a_1 D_1' + a_1 D_2' + a_3 D_3' + \sum_{i=1}^{N} A_i E_i' \\
&= a_1\Big(1 - \frac{S^*}{S}\Big)S' + a_2\Big(1 - \frac{I^*}{I}\Big)I' + a_3\Big(1 - \frac{B^*}{B}\Big)B' + \sum_{i=1}^{N} A_i\Big(1 - \frac{Z_i^*}{Z_i}\Big)Z_i' \\
&= a_1\beta_H S^* I^* \left(1 - \frac{S^*}{S} + \frac{I}{I^*} - \frac{SI}{S^*I^*} + \frac{\beta_L}{\beta_H}\left(\frac{B^* + B}{I^*} - \frac{SB}{S^*I^*} - \frac{S^*B^*}{SI^*}\right)\right) \\
&\quad + a_2\beta_H S^* I^* \left(1 - \frac{I}{I^*} - \frac{S}{S^*} + \frac{SI}{S^*I^*} + \frac{\beta_L}{\beta_H}\left(\frac{B^*}{I^*} - \frac{SB}{S^*I} + \frac{SB}{S^*I^*} - \frac{IB^*}{I^{*2}}\right)\right) \\
&\quad - a_3\frac{\alpha}{\kappa}(B - B^*)^2 + a_3\sum_{i=1}^{N} p_i\xi_i Z_i^*\left(1 - \frac{B}{B^*} + \frac{Zi}{Z_i^*} - \frac{Z_iB^*}{Z_i^*B}\right) \\
&\quad + \sum_{i=1}^{N} A_i\xi_i Z_i^*\left(1 - \frac{Z_i}{Z_i^*} + \frac{B}{B^*} - \frac{Z_i^*B}{Z_iB^*}\right) - a_1\mu\frac{(S - S^*)^2}{S} \\
&\leq a_1\beta_H S^* I^* \left(1 - \frac{S^*}{S} + \frac{I}{I^*} - \frac{SI}{S^*I^*} + \frac{\beta_L}{\beta_H}\left(\frac{B^* + B}{I^*} - \frac{SB}{S^*I^*} - \frac{S^*B^*}{SI^*}\right)\right) \\
&\quad + a_2\beta_H S^* I^* \left(1 - \frac{I}{I^*} - \frac{S}{S^*} + \frac{SI}{S^*I^*} + \frac{\beta_L}{\beta_H}\left(\frac{B^*}{I^*} - \frac{SB}{S^*I} + \frac{SB}{S^*I^*} - \frac{IB^*}{I^{*2}}\right)\right) \\
&\quad + a_3\sum_{i=1}^{N} p_i\xi_i Z_i^*\left(1 - \frac{B}{B^*} + \frac{Zi}{Z_i^*} - \frac{Z_iB^*}{Z_i^*B}\right) + \sum_{i=1}^{N} A_i\xi_i Z_i^*\left(1 - \frac{Z_i}{Z_i^*} + \frac{B}{B^*} - \frac{Z_i^*B}{Z_iB^*}\right).
\end{aligned}$$

Take $a_1 = a_2 = a_3 = 1$, and $A_i = p_i (i = 1, 2, ..., N)$. Then

$$\begin{aligned}
\mathcal{L}' \leq\ & \beta_H S^* I^* \left(2 - \frac{S^*}{S} - \frac{S}{S^*}\right) + \sum_{i=1}^{N} p_i\xi_i Z_i^*\left(2 - \frac{Z_iB^*}{Z_i^*B} - \frac{Z_i^*B}{Z_iB^*}\right) \\
& + \beta_L S^* B^*\left(2 + \frac{B}{B^*} - \frac{I}{I^*} - \frac{S^*}{S} - \frac{SI^*B}{S^*IB^*}\right).
\end{aligned}$$

By our assumption, the last term is non-positive. Moreover, $\mathcal{L}' = 0$ iff $S = S^*, I = I^*, B = B^*$. Thus, the largest invariant set for which $\mathcal{L}' = 0$ contains only X_2^*. Therefore, by LaSalle's Invariant Principle [34], X_2^* is globally asymptotically stable. ■

3.5 Numerical simulation

In this section, we conduct numerical simulation to our proposed multi-scale cholera model, both to verify our analytical results and to explore scenarios that are not covered in our analysis. To make distinction among hosts, we label all the individuals by integers from 1 to N. Thus, each individual is assigned a unique numeric ID that belongs to the set $\{1, 2, ..., N\}$. Our mathematical analysis is concerned with this scenario and Theorems 9 and 10 predict the global stabilities of the DFE and the endemic equilibrium, respectively.

In our numerical tests, we use the base values of the model parameters provided in Table **??**. Meanwhile, we set the initial conditions as follows:

$$I(0) = J,\ R(0) = 0,\ S(0) = N - I(0) - R(0),$$
$$B(0) = 10^4 \text{cells/ml},\ Z_i(0) = 0,$$

for $1 \leq i \leq N$, and some integer $J \geq 1$. For those individuals who are initially infected, $c_i \neq 0$ for$i \leq i \leq J$. Here, for simplicity, we assume that the individuals labeled with $i \leq i \leq J$ are initially infected. Thus, we set $c_i > 0$ for $i \leq i \leq J$, and $c_i = 0$ for $J + 1 \leq i \leq N$.

Figure 3.1 shows that each curve starts with a different initial condition, and all these curves converge to the DFE at $(B, I) = (0, 0)$, illustrating that the DFE is globally asymptotically stable when $\mathcal{R}_0 < 1$. In contrast, Figure 3.2 shows each curve starts with a different initial condition, and all these orbits approach the endemic equilibrium at $(S, I) = (410, 59)$, illustrating that the endemic equilibrium is globally asymptotically stable when $R_1 > 1$. In these two cases, we simply set $c_i = 2$ for $i = 1, 2, ..., J$. The

Table 3.1

Model parameters and values (p=person, d=day)

Parameter	Definition	Value	References
N	Total number of human individuals	10000p	Assumed
μ	Natural human birth/death rate	$(15878\text{d})^{-1}$	[40]
β_H	Direct transmission rate	$1.57 \times 10^{-5}\text{d}^{-1}$	[40]
β_L	Indirect transmission rate	$1.1 \times 10^{-8}\text{p}^{-1}\text{d}^{-1}$	[40]
γ	Recovery rate	0.2d^{-1}	[27]
c_i	Transfer rate	Varied	
ξ_i	Removal rate of human vibrios	10d^{-1}	Assumed
α	Bacterial growth rate	0.1d^{-1}	Assumed
κ	Bacterial carrying capacity	$10^6\text{cells}\cdot\text{ml}^{-1}$	[58]
p_i	Shedding rate	10%	Assumed
δ	Death rate of environmental vibrios	$(30\text{d})^{-1}$	[27]

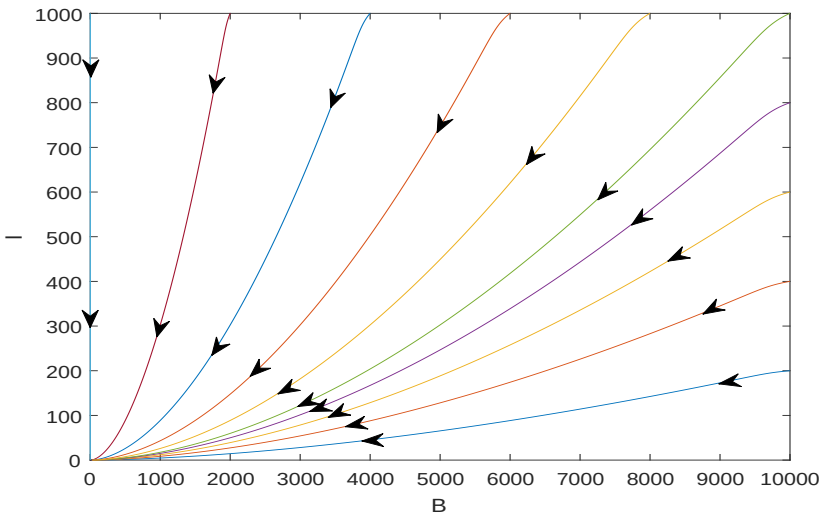

Figure 3.1

A typical phase portrait for I versus B when $\mathcal{R}_0 < 1$

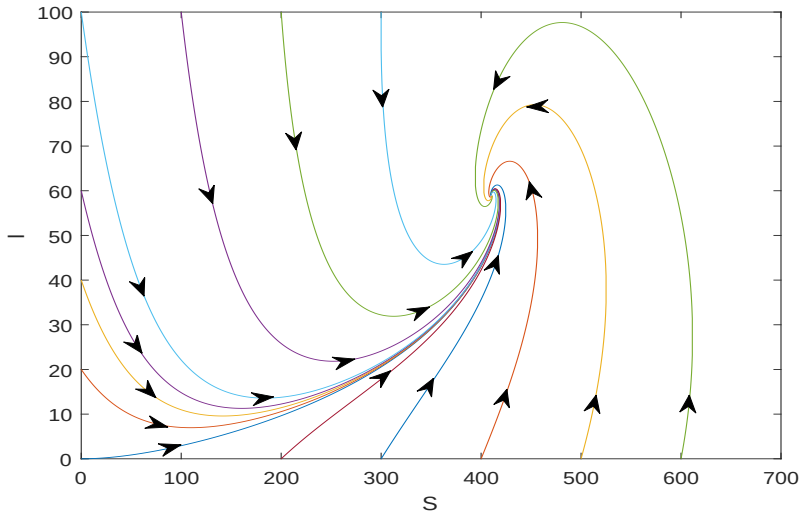

Figure 3.2

A typical phase portrait for I versus S when $R_1 > 1$

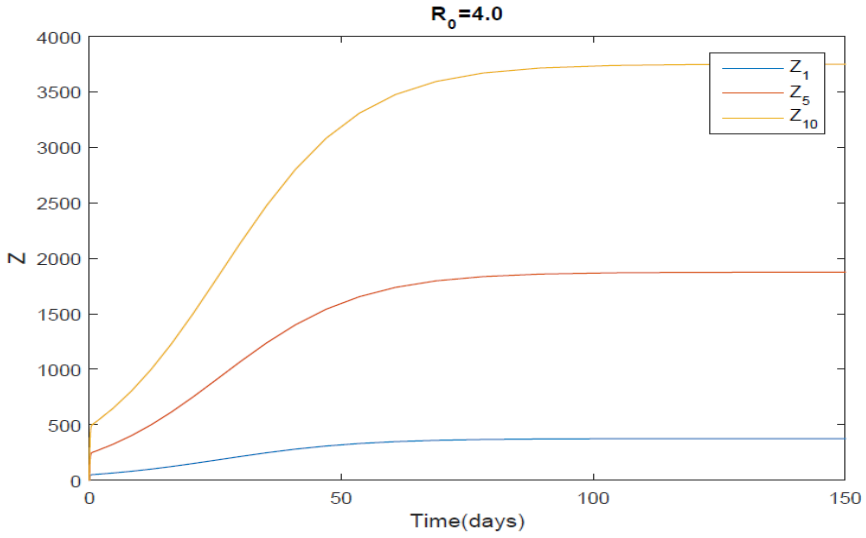

Figure 3.3

Z_i versus time for $i = 1, 5, 10$

results are consistent with the analytical predictions. Additionally, to examine the specific dynamical behavior of the human vibrios within different hosts, we set $c_i = 0.04i$ for $1 \leq i \leq J$, and $c_i = 0$ for $i > J$, with $J = 10$. Other parameter values remain the same. We then plot the time evolution of $Z_i(t)$ for a few typical (initially infected) individuals in Figure 3.3. We see that each curve starts from 0 and increases quickly during the first few hours, showing the fast increase of the pathogen load within the human body upon infection, then approaches a steady state. Among these curves, $Z_{10}(t)$ and $Z_1(t)$ attain the highest and lowest levels, due to that c_{10} and c_1 have the largest and smallest values, respectively. Moreover, each curve approaches a positive steady state over time, another evidence of the stability of the endemic equilibrium.

3.6 Discussion

In this chapter, we have focused our attention on the case where each model parameter is a constant independent of time. For this model, we are able to conduct a detailed mathematical analysis. We have shown the existence and uniqueness of the DFE and the endemic equilibrium and established their stabilities using threshold conditions based on the basic reproduction number. In particular, Rouché's Theorem helps us to prove the local stability of the endemic equilibrium, and the use of a Lyapunov function allows us to establish its global stability under some additional constraint. Our numerical simulation results are consistent with these analytical findings. The disease transmission at the population (or macroscopic) level impacts the pathogen load at the individual (or microscopic) level, whereas the variation of the pathogen concentrations inside the human body shapes the classifications of hosts (susceptible, infected, and recovered) and their interactions outside the human body. This study could be a starting point for establishing a comprehensive, adaptive modeling framework for cholera with a strong and consistent connection between the within-host and between-host dynamics.

CHAPTER 4

CHOLERA MODEL INCORPORATING MEDICAL RESOURCES

4.1 Model formulation and analysis

We use the following differential equations to describe the impact of available medical resources on cholera transmission:

$$\begin{aligned}
\frac{dS}{dt} &= \mu N - \beta_1(M)SI - \beta_2(M)S\frac{B}{B+K} - \mu S,\\
\frac{dI}{dt} &= \beta_1(M)SI + \beta_2(M)S\frac{B}{B+K} - (\gamma+\mu)I,\\
\frac{dR}{dt} &= \gamma I - \mu R,\\
\frac{dB}{dt} &= \xi(M)I - \delta B,\\
\frac{dM}{dt} &= -\Gamma + \eta I + \lambda(M).
\end{aligned} \tag{4.1.1}$$

Here S, I, and R are the the numbers of susceptible, infected, and recovered individuals, respectively, and B is the concentration of the pathogenic vibrios in the environment. Meanwhile, M denotes the strength (or, availability) of related medical resources and facilities, normalized to $0 \leq M \leq 1$; these could include, in a broad (and abstract) sense, medicines, health centers, sanitation systems, etc. The parameter μ is the natural birth and death rate for the human hosts, K is the half saturation concentration of the vibrios, γ is the rate of recovery from cholera infection, and δ is the removal rate of vibrios from the environment. We neglect the disease induced death rate in our model, since the mortality rate for cholera is generally lower than 1% [66]; in particular, the overall case fatality rate for the Yemen cholera outbreak from April 2017 to May 2018 is 0.21% [70].

The parameter Γ represents the outflux rate of the medical resources due to

socioeconomic factors such as conflicts, wars, and economic collapse. Meanwhile, the availability of medical resources is stimulated by the disease prevalence at a rate η (for example, through international assistance from WHO, CDC, UNICEF, etc.). We additionally assume that its self growth is described by a function $\lambda(M)$, which is introduced to ensure that a positive number of medical facilities and infrastructures are available at any time, as a minimal requirement of public health. The parameters β_1 and β_2 are the direct (or, human-to-human) and indirect (or, environment-to-human) transmission rates, respectively, and ξ is the rate of human contribution (e.g., through shedding) to the environmental vibrios. We assume that β_1 , β_2 and ξ all explicitly depend on M and increase while M decays, reflecting the impact of the collapsing public infrastructure on cholera transmission and spread. Specifically, we make the following assumptions on these three parameters:

(H1) $\beta_1(M)$, $\beta_2(M)$, $\xi(M) \in C^1[0,1]$ and are all positive;

(H2) $\beta_1'(M) \leq 0,\ \beta_2'(M) \leq 0,\ \xi'(M) \leq 0.$

We also assume that the function $\lambda(M)$ satisfies:

(H3) $\lambda(M) \in C^1[0,1]$ and $\lambda'(M) < 0$;

(H4) $\lambda(0) > \Gamma > \eta N + \lambda(1)$.

The condition (H3) states that when the available medical resource (M) increases, its self-growth rate would decrease. The condition (H4) is introduced to ensure that M remains in the range $[0,1]$.

4.1.1 Basic reproduction number

We continue to use the basic reproduction number in the analysis of our model (4.1.1). Let us first determine $\mathcal{R}_0$ by the standard next generation matrix technique. Note that $\lambda(M)$ is invertible since $\lambda'(M) < 0$. The model (4.1.1) has a unique disease-

free equilibrium (DFE) at

$$E_0 = (S_0, I_0, R_0, B_0, M_0) = \big(N, 0, 0, 0, \lambda^{-1}(\Gamma)\big). \tag{4.1.2}$$

The infection components in this model are I and B. We find that the new infection matrix F and the transition matrix V are given by

$$F = \begin{bmatrix} \beta_1(M_0)N & \beta_2(M_0)N/K \\ 0 & 0 \end{bmatrix} \quad \text{and} \quad V = \begin{bmatrix} \gamma+\mu & 0 \\ -\xi(M_0) & \delta \end{bmatrix}. \tag{4.1.3}$$

It follows that the next generation matrix is given by

$$FV^{-1} = \begin{bmatrix} \frac{\beta_1(M_0)N}{\gamma+\mu} + \frac{\beta_2(M_0)\xi(M_0)N}{\delta K(\gamma+\mu)} & \frac{\beta_2(M_0)N}{\delta K} \\ 0 & 0 \end{bmatrix}. \tag{4.1.4}$$

The basic reproduction number of model (4.1.1) is then defined as the spectral radius of the matrix FV^{-1}, and we find that

$$\mathcal{R}_0 = \rho(FV^{-1}) = \frac{\beta_1(M_0)N}{\gamma+\mu} + \frac{\beta_2(M_0)\xi(M_0)N}{\delta K(\gamma+\mu)} =: \mathcal{R}_{01} + \mathcal{R}_{02}\,, \tag{4.1.5}$$

which provides a quantification of the disease risk during a cholera outbreak. The first term $\mathcal{R}_{01}$ comes from the direct transmission route, and the second term $\mathcal{R}_{02}$ represents the contribution from the indirect transmission route.

4.1.2 Equilibria analysis

We now analyze the equilibria of the model (4.1.1) which will provide essential information regarding the transmission dynamics of the disease. Let (S, I, R, B, M) be

an equilibrium of model (4.1.1), which satisfies the following equations:

$$\begin{aligned}
&\mu N - \beta_1(M)SI - \beta_2(M)S\frac{B}{B+K} - \mu S \;=\; 0,\\
&\beta_1(M)SI + \beta_2(M)S\frac{B}{B+K} - (\gamma+\mu)I \;=\; 0,\\
&\gamma I - \mu R \;=\; 0,\\
&\xi(M)I - \delta B \;=\; 0,\\
&-\Gamma + \eta I + \lambda(M) \;=\; 0.
\end{aligned} \tag{4.1.6}$$

Solving (4.1.6) yields

$$\begin{aligned}
S &= \frac{(\gamma+\mu)I}{\beta_1(M)I + \beta_2(M)B/(B+K)},\\
M &= \lambda^{-1}(\Gamma - \eta I),\\
R &= \frac{\gamma}{\mu}I,\\
B &= \frac{\xi(M)}{\delta}I.
\end{aligned} \tag{4.1.7}$$

Note that $\Gamma - \eta I > 0$ based on the condition (H4). It follows from $S + I + R = N$ that the third equation of (4.1.7) implies

$$S = N - aI =: \phi(I) \quad \text{with} \quad a = 1 + \gamma/\mu. \tag{4.1.8}$$

Meanwhile, in view of the first equation of (4.1.7), we obtain

$$S = \frac{\gamma+\mu}{h(I)} =: \psi(I), \tag{4.1.9}$$

where

$$h(I) = \beta_1(\chi(I)) + \frac{\beta_2(\chi(I))\,\xi(\chi(I))}{\xi(\chi(I))\,I + \delta K} \quad \text{with} \;\; \chi(I) = \lambda^{-1}(\Gamma - \eta I). \tag{4.1.10}$$

Consider curves $S = \phi(I)$ and $S = \psi(I)$. In particular, any intersection of these two curves in $\mathbb{R}^2_+$ determines a non-DFE equilibrium. Note that

$$\begin{aligned} h'(I) =& \beta_1'(\chi(I))\chi'(I) + \frac{\beta_2'(\chi(I))\,\chi'(I)\,\xi(\chi(I))}{\xi(\chi(I))\,I + \delta K} \\ &+ \beta_2(\chi(I))\frac{\delta K\xi'(\chi(I))\chi'(I) - \xi^2(\chi(I))}{(\xi(\chi(I))\,I + \delta K)^2}\,. \end{aligned} \tag{4.1.11}$$

Using assumption (H2) and the fact $\chi'(I) = -\eta/\lambda'(\chi(I)) > 0$, we see that $h'(I) \leq 0$. This implies that $\psi(I)$ is an increasing function. In contrast, $\phi(I)$ is strictly decreasing. Additionally, one can easily verify that $\psi(0) = N/\mathcal{R}_0$, $\phi(0) = N$, $\psi(N/a) > 0$ and $\phi(N/a) = 0$. Hence, we conclude:

(1) If $\mathcal{R}_0 > 1$, these two curves have a unique intersection lying in the interior of $\mathbb{R}^2_+$, due to $\psi(0) < \phi(0)$ and $\psi(N/a) > \phi(N/a)$. Furthermore, at this intersection point, equation (4.1.7) yields $M, R, B > 0$ (since $I > 0$).

(2) If $\mathcal{R}_0 \leq 1$, the two curves have no intersection in the interior of $\mathbb{R}^2_+$ as $\psi(0) \geq \phi(0)$.

Therefore, by equation (4.1.7), we find that the model (4.1.1) admits a unique equilibrium, the DFE, if $\mathcal{R}_0 \leq 1$; and it admits two equilibria, the DFE and an endemic equilibrium (EE), if $\mathcal{R}_0 > 1$.

In what follows, we perform a study on the global stability of the DFE. By a simple comparison principle, we find that $0 \leq B \leq B_{max}$ and $M_0 \leq M \leq 1$, where $B_{max} = \xi(0)N/\delta$. Thus, it leads to a biological feasible domain

$$\Omega = \{(S, I, R, B, M) \in \mathbb{R}^5_+ : S + I + R = N,\, 0 \leq B \leq B_{max},\, M_0 \leq M \leq 1\}.$$

Theorem 11. *The following statements hold for the model* (4.1.1).

(1) *If* $\mathcal{R}_0 \leq 1$, *the DFE of the model* (4.1.1) *is globally asymptotically stable in* Ω.

(2) *If* $\mathcal{R}_0 > 1$, *the DFE of the model* (4.1.1) *is unstable and there exists a unique endemic equilibrium. Moreover, the disease is uniformly persistent in the interior of* Ω, *denoted by* $\mathring{\Omega}$; *namely,* $\liminf_{t\to\infty}(I(t), B(t)) > (c, c)$ *for some* $c > 0$.

Proof. Let $\mathbf{x} = (I, B)^T$. One can verify that

$$\frac{d\mathbf{x}}{dt} \leq (F - V)\mathbf{x},$$

where the matrices F and V are given in equation (4.1.3). Take

$$\mathbf{u} = (\beta_1(M_0)N,\ \beta_2(M_0)N/K).$$

It then follows from the fact $\mathcal{R}_0 = \rho(FV^{-1}) = \rho(V^{-1}F)$ that $\mathbf{u}$ is a left eigenvector associated with the eigenvalue $\mathcal{R}_0$ of the matrix $V^{-1}F$; i.e., $\mathbf{u}V^{-1}F = \mathcal{R}_0\mathbf{u}$. Let us consider the Lyapunov function

$$\mathcal{L} = \mathbf{u}V^{-1}\mathbf{x}.$$

Differentiating $\mathcal{L}$ along the solutions of (4.1.1), we have

$$\mathcal{L}' = \mathbf{u}V^{-1}\mathbf{x}' \leq \mathbf{u}V^{-1}(F - V)\mathbf{x} = \mathbf{u}(\mathcal{R}_0 - 1)\mathbf{x}. \tag{4.1.12}$$

Case 1: $\mathcal{R}_0 < 1$. The equality $\mathcal{L}' = 0$ implies that $\mathbf{ux} = 0$. This leads to $I = B = 0$ by noting the positive components of $\mathbf{u}$. Hence, when $\mathcal{R}_0 < 1$, equations of (4.1.6) yield $S = S_0,\ M = M_0$ and $I = R = B = 0$. Therefore, the invariant set on which $\mathcal{L}' = 0$ contains only one point which is the DFE.

Case 2: $\mathcal{R}_0 = 1$. The equality $\mathcal{L}' = 0$ implies that $\beta_1(M)SI = \beta_1(M_0)NI$, $\beta_2(M)SB/(B + K) = \beta_2(M_0)NB/K$ and $\xi(M)I = \xi(M_0)I$. Thus, either $I = B = 0$, or $B = 0$, $S = N$ and $\beta_1(M) = \beta_1(M_0)$ and $\xi(M) = \xi(M_0)$ hold. The former can proceed as above. Suppose the latter holds, then $\frac{dB}{dt} = \xi(M)I \equiv 0$ which implies $I = 0$. Once again this would yield the same conclusion as before.

Therefore, in either case, the largest invariant set on which $\mathcal{L}' = 0$ consists of the singleton $E_0 = (N, 0, 0, 0, M_0)$. By LaSalle's Invariant Principle [34], the DFE is globally asymptotically stable in Ω if $\mathcal{R}_0 \leq 1$.

In contrast, if $\mathcal{R}_0 > 1$, then it follows from the continuity of vector fields that

$\mathcal{L}' > 0$ in a neighborhood of the DFE in $\mathring{\Omega}$. Thus the DFE is unstable by the Lyapunov stability theory. The last part can be proved by the persistent theory [51] that is similar to the proof of Theorem 2.5 in Gao and Ruan [24]. ■

In addition, we have carried out an analysis on the global asymptotic stability of the endemic equilibrium. We remark that, in general, this would be a nontrivial task for an epidemic system of dimension higher than two. Our model (4.1.1) is essentially four-dimensional, after we remove the equation for R. We have managed to conduct the endemic stability analysis using the geometric approach based on the third additive compound matrix [37]. We briefly describe this method in the following.

The third additive compound matrix for a 4×4 matrix $A = (a_{ij})$ is defined as

$$A^{[3]} = \begin{bmatrix} a_{11}+a_{22}+a_{33} & a_{34} & -a_{24} & a_{14} \\ a_{43} & a_{11}+a_{22}+a_{44} & a_{23} & -a_{13} \\ -a_{42} & a_{32} & a_{11}+a_{33}+a_{44} & a_{12} \\ a_{41} & -a_{31} & a_{21} & a_{22}+a_{33}+a_{44} \end{bmatrix}.$$

Now consider a dynamical system

$$\frac{dX}{dt} = F(X), \tag{4.1.13}$$

where $F : D \mapsto \mathbb{R}^n$ is a C^1 function and where $D \subset \mathbb{R}^n$ is a simply connected open set. Let $X(t, X_0)$ denote the solution of (4.1.13) with the initial condition $X(0) = X_0$. We make two assumptions.

(a1) There exists a compact absorbing set $K \subset D$;

(a2) The system (4.1.13) has a unique equilibrium point X^* in D.

The linearized system of equation (4.1.13) is

$$Y' = J(X(t, X_0))Y, \tag{4.1.14}$$

and the associated third compound system is

$$Z' = J^{[3]}(X(t, X_0))Z\,, \tag{4.1.15}$$

where $J^{[3]}$ is the third compound matrix of the Jacobian J for equation (4.1.13).

Theorem 12. *Assume that (a1), (a2) hold and there are a Lyapunov function $V(X, Z)$, a function $\kappa(t)$, and positive constants c, k, and C such that*

(i) $c|Z| \le V(X, Z) \le C|Z|,\ c \le \kappa(t) \le C$;

(ii) $V' \le (\kappa'(t) - k)V$,

where the total derivative V' is taken along the direction of (4.1.15)*. Then the interior equilibrium X^* of system* (4.1.13) *is globally asymptotically stable.*

Proof. If $\kappa(t)$ is a constant, this is the case covered by Corollary 3.2 in [37]. For a general differentiable function $\kappa(t)$, the conclusion follows from a similar proof, since the modified Lyapunov function $\tilde{V} = V(X, Z)/\kappa(t)$ satisfies all the conditions to establish Corollary 3.2 in [37]. ■

We now prove the main result in this section; i.e., the global stability of the endemic equilibrium, using the geometric approach described above. To simplify our notations, we will adopt the abbreviations

$$\beta_1 = \beta_1(M), \quad \beta_2 = \beta_2(M), \quad \xi = \xi(M), \quad \lambda = \lambda(M).$$

Furthermore, we will assume that each of these four functions is subject to saturation effects, a common assumption for disease-related rates, mathematically characterized by a non-positive second derivative.

Theorem 13. *If $\mathcal{R}_0 > 1$ and the following inequalities hold for all $M \in [0,\ 1]$*

$$\beta_1'', \beta_2'', \xi'', \lambda'' \le 0 \ \text{ and } \ \beta_1 \le \frac{\mu}{N}, \tag{4.1.16}$$

then the unique endemic equilibrium of the system (4.1.1) *is globally asymptotically stable in* $\mathring{\Omega}$.

Proof. It is clear that the equation for R can be decoupled from the system (4.1.1). As a result, we obtain a four-dimensional system associated with S, I, B, and M, for which the Jacobian matrix is given by

$$J = \begin{bmatrix} -\beta_1 I - \frac{\beta_2 B}{B+K} - \mu & -\beta_1 S & \frac{-\beta_2 SK}{(B+K)^2} & -\beta_1' SI - \frac{\beta_2' SB}{B+K} \\ \beta_1 I + \frac{\beta_2 B}{B+k} & \beta_1 S - (\gamma+\mu) & \frac{\beta_2 SK}{(B+K)^2} & \beta_1' SI + \frac{\beta_2' SB}{B+K} \\ 0 & \xi & -\delta & \xi' I \\ 0 & \eta & 0 & \lambda' \end{bmatrix}.$$

The third additive compound matrix of J is

$$J^{[3]} = \begin{bmatrix} a_1 & \xi' I & -\beta_1' SI - \frac{\beta_2' SB}{B+K} & -\beta_1' SI - \frac{\beta_2' SB}{B+K} \\ 0 & a_2 & \frac{\beta_2 SK}{(B+K)^2} & \frac{\beta_2 SK}{(B+K)^2} \\ -\eta & \xi & a_3 & -\beta_1 S \\ 0 & 0 & \beta_1 I + \frac{\beta_2 B}{B+K} & a_4 \end{bmatrix},$$

where

$$\begin{aligned} a_1 &= \beta_1 S - \beta_1 I - \frac{\beta_2 B}{B+K} - \gamma - 2\mu - \delta, \\ a_2 &= \beta_1 S - \beta_1 I + \lambda' - \frac{\beta_2 B}{B+K} - \gamma - 2\mu, \\ a_3 &= \lambda' - \beta_1 I - \frac{\beta_2 B}{B+K} - \mu - \delta, \\ a_4 &= \lambda' + \beta_1 S - \gamma - \mu - \delta. \end{aligned}$$

The associated linear compound system is

$$\begin{aligned}
X' &= a_1 X + \xi' IY - (\beta_1' SI + \frac{\beta_2' SB}{B+K})Z - \left(\beta_1' SI + \frac{\beta_2' SB}{B+K}\right) W, \\
Y' &= a_2 Y + \frac{\beta_2 SK}{(B+K)^2} Z + \frac{\beta_2 SK}{(B+K)^2} W, \\
Z' &= -\eta X + \xi Y + a_3 Z - \beta_1 SW, \\
W' &= \left(\beta_1 I + \frac{\beta_2 B}{B+K}\right) Z + a_4 W.
\end{aligned} \tag{4.1.17}$$

We need to show the uniform global stability of the linear compound system (4.1.17). To this end, we choose an associated Lyapunov function

$$V(t, X, Y, Z, W) = \max(V_1, V_2, V_3),$$

where

$$V_1 = M|X|, \quad V_2 = B|Y|, \quad V_3 = \begin{cases} I|Z+W|, & ZW \geq 0, \\ \max(I|Z|, I|W|), & ZW < 0. \end{cases}$$

It is easy to see that the following estimate holds

$$I|Z+W| \leq V_3 \leq V, \quad (Z,\ W) \in \mathbb{R}^2. \tag{4.1.18}$$

Based on the uniform persistence of the system, we see that there exist positive constants c_1 and c_2 such that

$$c_1(|X| + |Y| + |Z| + |W|) \leq V \leq c_2(|X| + |Y| + |X| + |W|). \tag{4.1.19}$$

Meanwhile, note that $\beta_1,\ \beta_2 > 0$ for $M \in [0,\ 1]$, we can choose a small positive constant k such that

$$\beta_1 I + \frac{\beta_2 B}{B+K}, \quad \gamma,\ \mu \geq k. \tag{4.1.20}$$

Other than that, we have the following inequalities by (4.1.16):

$$\begin{aligned} &\beta_1 S \le \mu, \ \ -\xi' M \le \xi, \ \ -\beta_2' M \le \beta_2 \,, \\ &\lambda' \le \frac{\lambda - \lambda(0)}{M} \le \frac{\lambda - \Gamma}{M} \le \frac{M'}{M} \,. \end{aligned} \tag{4.1.21}$$

Now, we can estimate the total derivative of V along the trajectory of the compound system (4.1.17) by inequalities (4.1.20) and (4.1.21). We need to discuss the following cases.

Case 1: $V = V_1$. Then $B|Y| \le M|X|,\ I|Z+W| \le M|X|$. We have

$$\begin{aligned} D_+V &= M'|X| + MD_+|X| \\ &\le M'|X| + M\left(a_1|X| - \xi' I|Y| - \left(\beta_1' SI + \frac{\beta_2' SB}{B+K}\right)|Z+W|\right) \\ &\le \left(\frac{M'}{M} + a_1 - \frac{\xi' MI}{B} - \frac{\beta_2' MSB}{(B+K)I} - \beta_1' MS\right) V \\ &\le \left(\frac{M'}{M} + 2\beta_1 S + \frac{\beta_2 SB}{(B+K)I} - \gamma - 2\mu + \frac{\xi I}{B} - \delta - \left(\beta_1 I + \frac{\beta_2 B}{B+K}\right)\right) V \\ &\le \left(\frac{M'}{M} + \frac{I'}{I} + \frac{B'}{B} - k\right) V. \end{aligned} \tag{4.1.22}$$

Case 2: $V = V_2$. Then $I|Z+W| \le B|Y|$, and

$$\begin{aligned} D_+V &= B'|Y| + BD_+|Y| \\ &\le B'|Y| + B\left(a_2|Y| + \frac{\beta_2 SK}{(B+K)^2}|Z+W|\right) \\ &\le \left(\frac{B'}{B} + \beta_1 S + \frac{\beta_2 SBK}{(B+K)^2 I} - \gamma - 2\mu + \lambda' - \left(\beta_1 I + \frac{\beta_2 B}{B+K}\right) -\right) V \\ &\le \left(\frac{B'}{B} + \frac{I'}{I} + \frac{M'}{M} - k\right) V. \end{aligned} \tag{4.1.23}$$

Case 3-a: $V = I|Z+W|$. Then $M|X|, B|Y| \leq I|Z+W|$, and

$$\begin{aligned} D_+V &= I'|Z+W| + ID_+|Z+W| \\ &\leq I'|Z+W| + I(\eta|X| + \xi|Y| + (\lambda' - \mu - \delta)|Z+W| - \gamma|W|) \\ &\leq \left(\frac{I'}{I} + \frac{\xi I}{B} - \delta + \frac{\eta I}{M} + \lambda' - \mu\right) V \\ &\leq \left(\frac{I'}{I} + \frac{B'}{B} + \frac{\lambda - \Gamma + \eta I}{M} - \mu\right) V \\ &\leq \left(\frac{I'}{I} + \frac{B'}{B} + \frac{M'}{M} - k\right) V. \end{aligned} \tag{4.1.24}$$

Case 3-b: $V = I|Z|$. Then $|W| \leq |Z|, M|X|, B|Y| \leq I|Z|$, and

$$\begin{aligned} D_+V &= I'|Z| + ID_+|Z| \\ &\leq I'|Z| + I\left(\eta|X| + \xi|Y| + \left(\lambda' - \beta_1 I - \frac{\beta_2 B}{B+K} - \mu - \delta\right)|Z| + \beta_1 S|W|\right) \\ &\leq \left(\frac{I'}{I} + \frac{\xi I}{B} - \delta + \frac{\eta I}{M} + \lambda' - \left(\beta_1 I + \frac{\beta_2 B}{B+K}\right) + \beta_1 S - \mu\right) V \\ &\leq \left(\frac{I'}{I} + \frac{B'}{B} + \frac{M'}{M} - k\right) V. \end{aligned} \tag{4.1.25}$$

Case 3-c: $V = I|W|$. Then

$$\begin{aligned} D_+V &= I'|W| + ID_+|W| \\ &= I'|W| + I\left(-\left(\beta_1 I + \frac{\beta_2 B}{B+K}\right)|Z| + (\lambda' + \beta_1 S - \gamma - \mu - \delta)|W|\right) \\ &\leq \left(\frac{I'}{I} + \lambda' - \delta - \gamma + \beta_1 S - \mu\right) V \\ &\leq \left(\frac{I'}{I} + \frac{M'}{M} + \frac{\xi I}{B} - \delta - \gamma\right) V \\ &\leq \left(\frac{I'}{I} + \frac{M'}{M} + \frac{B'}{B} - k\right) V. \end{aligned} \tag{4.1.26}$$

Now, let $\kappa(t) = \ln(IBM)$. Then it follows from (4.1.22) to (4.1.26) that the following inequality holds

$$D_+|V| \leq (\kappa(t)' - k)V. \tag{4.1.27}$$

In view of the uniform persistence, we can actually choose c_1 and c_2 from (4.1.19) such that

$$c_1 \leq \kappa(t) \leq c_2, \tag{4.1.28}$$

for sufficiently large t. Therefore, we conclude from (4.1.19), (4.1.27), (4.1.28) and Theorem 12 that the endemic equilibrium of the system (4.1.1) is globally asymptotically stable. ■

Essentially, the stability results in Theorems 11 and 13 establish $\mathcal{R}_0 = 1$ as a forward transcritical bifurcation point, or, a sharp threshold for disease dynamics, and indicate that reducing $\mathcal{R}_0$ to values at or below unity will be sufficient to eradicate the disease. In other words, the cholera model (4.1.1) exhibits *regular* threshold dynamics.

4.2 Numerical results

In order to verify our mathematical modeling framework, we apply our model to study the recent cholera outbreak in Yemen, where heavy conflicts and wars have led to a collapsed public health system and severe shortage of medical resources. Using our model, we aim to gain insight into the transmission pattern of this large-scale cholera outbreak under the impact of limited medical resources.

We utilize the outbreak data in the Yemen Situation Reports published weekly by WHO [71]. These data sets contain the weekly reported new cases and cumulative cases for each governorate as well as the entire country. We implement our model and conduct numerical simulation for an epidemic period slightly over one year, starting from April 2017 (when the cholera epidemic resurged in Yemen and went on to become the worst cholera outbreak in modern history) and ending in May 2018 (when the cholera epidemic significantly slowed down already and only a small number of new cases were reported since then).

We first describe how the values of the model parameters are determined in our numerical simulation. The entire population in Yemen is about $N = 27.5$ million as of

2016 [72]. The average life expectancy in Yemen is about 64 years [67], and so we may estimate the natural human death rate μ by $\mu \approx (64 \text{ year})^{-1} \approx 0.0003 \text{ week}^{-1}$. *Vibrio cholerae* can typically survive in the aquatic environment for about 30 days [42], thus we calculate the natural death (or, removal) rate of the bacteria by $\delta \approx (30 \text{ day})^{-1} \approx 0.233 \text{ week}^{-1}$. An individual with a moderate cholera infection could recover in about 5 days [27], and so we estimate the recovery rate by $\gamma \approx (5 \text{ day})^{-1} \approx 1.4 \text{ week}^{-1}$. Based on the recent WHO survey on Yemen's health system [69], only 45% of the medical facilities in Yemen remain fully functional after two years of wars. Then we may roughly estimate the decay rate of the medical resources by $\Gamma \approx 0.5 * 0.55 \text{ year}^{-1} \approx 0.00529 \text{ week}^{-1}$. Additionally, the half saturation rate of *Vibrio cholerae* is commonly accepted as $K \approx 10^6 \text{ cells} \cdot \text{ml}^{-1}$ [27].

On the other hand, the direct transmission rate $\beta_1(M)$, the indirect transmission rate $\beta_2(M)$, the average individual shedding rate $\xi(M)$, and the self-growth rate of medical resources $\lambda(M)$ all depend on M (where $0 \leq M \leq 1$) and are more difficult to calibrate. For simplicity, we consider the following representations of these rates, as decreasing functions of M:

$$\beta_1(M) = c_1 - d_1 M, \;\; \beta_2(M) = c_2 - d_2 M,$$
$$\xi(M) = c_3 - d_3 M, \;\; \lambda(M) = c_4 - d_4 M.$$

Using the base values from [40] for the cholera transmission rates and individual shedding rate, we set the lower bounds of these parameters as $\beta_1(1) = c_1 - d_1 = 1.099 \times 10^{-4} \text{ week}^{-1} \text{person}^{-1}$, $\beta_2(1) = c_2 - d_2 = 0.0077 \text{ week}^{-1}$, and $\xi(1) = c_3 - d_3 = 70 \text{ cells} \cdot \text{ml}^{-1} \text{week}^{-1} \text{person}^{-1}$. By using these conditions as well as the assumption (H4), we are left with five independent parameters c_i $(1 \leq i \leq 4)$ and η, whose values will then be determined through data fitting.

We conduct data fitting to a number of time series that include the weekly reported cases at the country level and the individual governorate level, based on the standard least squires method. We also note that the country of Yemen can be divided into three

major regions (the Northwest, the Southwest, and the East) which differ from each other in climatic and geographical conditions [65, 73]. The three regions can be roughly defined as follows:

- East: Longitude + Latitude $> 60°$;
- Northwest: Longitude + Latitude $< 60°$ & Latitude $> 14.5°$;
- Southwest: Longitude + Latitude $< 60°$ & Latitude $< 14.5°$.

In our numerical simulation, we have chosen one or more governorates from each of the three regions.

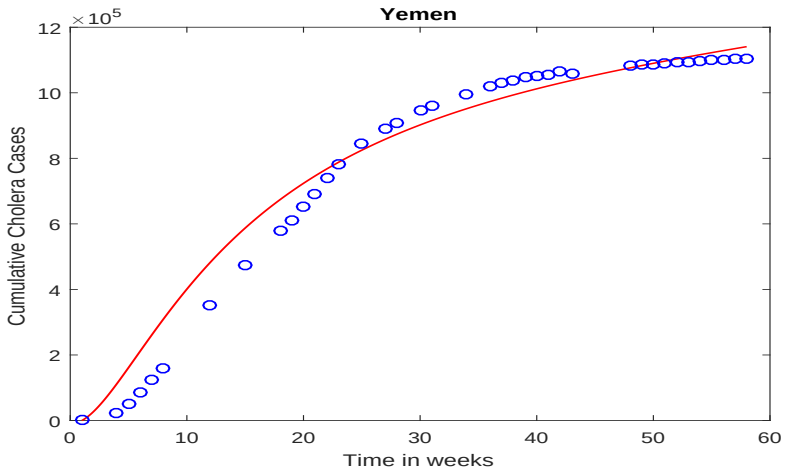

Figure 4.1

Curve fitting for Yemen from April 2017 to May 2018

We present the parameter values and their confidence intervals in the tables below (Tables 4.2-4.6) for the cholera data fitting of Yemen and its four governorates: Al Hudaydah in the Northwest, Taizz in the Southwest, and Al Jawf and Sa'ada in the East. The 95% confidence intervals listed in these tables imply that the corresponding p-values are greater than 0.05. They also indicate that the standard deviations are large. This may be caused by the fact that our sample size is relatively small, as our data fitting is based on the weekly reported cases from WHO for about 39 weeks in the period from

April 2017 to May 2018 (there are a number of weeks in this period that WHO did not report the data).

Table 4.1

The NMSE for the cholera data fitting of Yemen and its four governorates

	Yemen	Al Hudaydah	Taizz	Al Jawf	Sa'ada
NMSE	0.00615	0.01014	0.00590	0.03430	0.16661

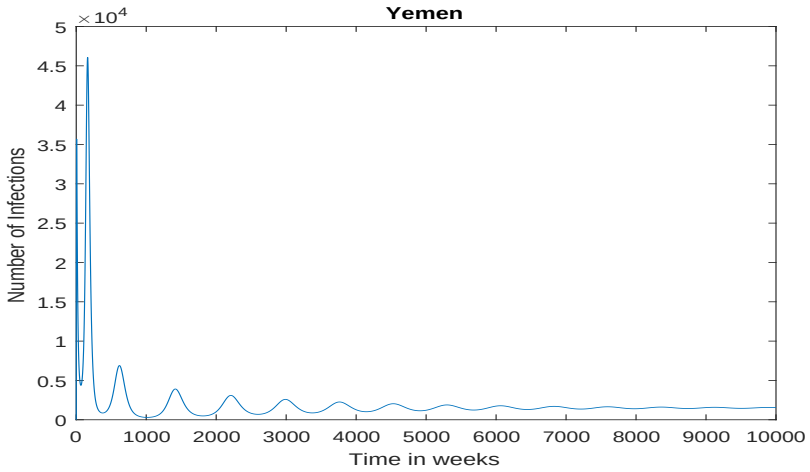

Figure 4.2

Long-term behavior of the infection in Yemen

Figure 4.1 shows the number of cumulative infections from the WHO reports and from our numerical simulation, for the entire country of Yemen. The parameters c_i $(1 \leq i \leq 4)$ and η are determined from the data fitting; their values and 95% confidence intervals are shown in Table 4.2. The basic reproduction number is estimated as $\mathcal{R}_0 = 1.344$. From Figure 4.1, we observe reasonably good fitting results based on our numerical simulation (red curve) to the reported data (blue circles). To quantify the goodness of fit, we have calculated the Normalized Mean Square Error (NMSE), which provides an estimate of the overall deviation between the predicted and measured values. The NMSE

in this case is computed by

$$\frac{1}{n}\sum_{i=1}^{n}\frac{(y_i - x_i)^2}{\bar{x}\bar{y}},$$

where

$$\bar{x} = \frac{1}{n}\sum_{i=1}^{n} x_i \text{ and } \bar{y} = \frac{1}{n}\sum_{i=1}^{n} y_i,$$

and x_i $(1 \leq i \leq n)$ are the WHO reported data, y_i $(1 \leq i \leq n)$ are the fitted data, and n is the number of data points used. In general, a lower value of NMSE indicates a better fitting result. The values of the NMSE for the cholera data fitting of Yemen (as well as four of its governorates) are presented in Table 4.1.

Table 4.2

Parameter values and confidence intervals for Yemen

Parameter	Value	95% Confidence Interval
c_1	0.000154	[0, 0.000526]
c_2	0.007759	[0, 0.05321]
c_3	1129.26	[0, 21482.8]
c_4	0.005518	[0, 0.797561]
η	0.00000012	[0, 0.00427212]

In Figure 4.1, we see that the the increase of the cumulative cholera cases was very fast during the first 20 weeks or so (starting from April 27, 2017), but gradually slowed down afterwards (ending in May 2018). Based on the data fitting result, we are able to evaluate the basic reproduction number from equation (4.1.5). We find that $\mathcal{R}_0 = 1.344$, consistent with our prediction of a cholera epidemic when $\mathcal{R}_0 > 1$. Moreover, Figure 4.2 is a numerical simulation for the number of cholera infections in Yemen, based on parameter values from data fitting, over a large time frame. It shows the long-term behavior of the infection (or, prevalence) curve which approaches a positive endemic state (i.e., the endemic equilibrium) over time, an evidence for the global stability of the endemic equilibrium when $\mathcal{R}_0 > 1$, as predicted by Theorem 13.

In order to conduct a deeper investigation into the transmission dynamics of this cholera outbreak, we have also carried out numerical simulation and data fitting for a

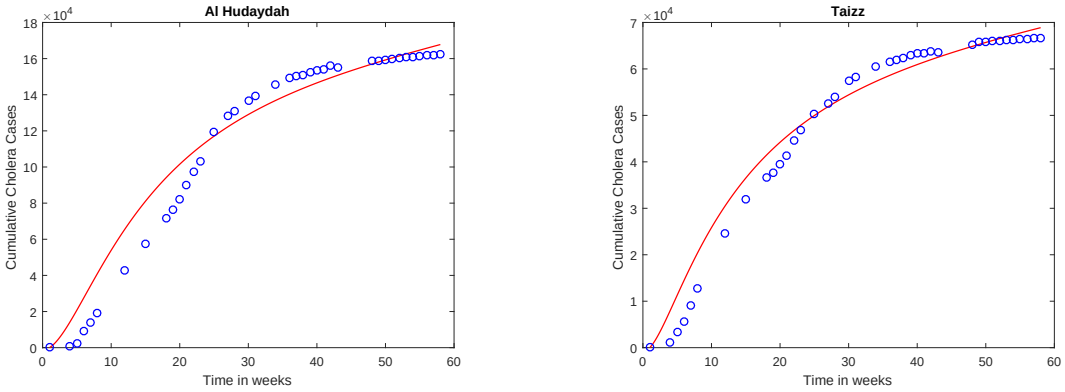

Figure 4.3

Curve fittings for Al Hudaydah and Taizz

number of individual governorates in Yemen. Figures 4.3 and 4.4 show some typical results, where one governorate is chosen from each of the Northwest and Southwest regions, and two chosen from the East region. The parameter values for c_i $(1 \leq i \leq 4)$ and η are again determined through data fitting in each scenario; see Tables 4.3 - 4.6 for their values and confidence intervals. We also calculate the values of $M_0, \mathcal{R}_{01}, \mathcal{R}_{02}$, and $\mathcal{R}_0$, which are provided in Table 4.7. We observe that Al Hudaydah in the Northwest has the highest cumulative infection cases among the four governorates, followed by Taizz in the Southwest, and the lowest are Al Jawf and Sa'ada in the East. Correspondingly, the value of the basic reproduction number $\mathcal{R}_0$ (evaluated based on the data fitting result for each governorate) is the highest for Al Hudaydah, and the lowest for Al Jawf and Sa'ada, indicating the different levels of disease risk in these places. More specifically, the numbers of cumulative cases in Al Jawf and Sa'ada are about one order lower than those in Al Hudaydah and Taizz. For each of the two governorates in the East, the reported number of cumulative cases remains pretty flat during the first 10 weeks or so, indicating that the onset of the major cholera outbreak in the East region lags behind, and is possibly caused by, that in the Northwest and Southwest regions. Meanwhile, when $t \geq 30$ weeks, the reported cumulative cases in Al Jawf and Sa'ada essentially level off, a strong indication that the cholera epidemic has been contained in these places after about 30 weeks. As a result, the reported cumulative cases in each of these two governorates in the East

(especially Sa'ada) show an approximate 'S' shape. These factors contribute to the fact that our least squares data fitting results for the eastern governorates (especially Sa'ada) are not as good as those for the northwestern and southwestern governorates. Indeed, Table 4.1 shows the values of the NMSE for each case, which quantifies the goodness of fitting, and we clearly observe that the NMSE value for Sa'ada is the highest, followed by that for Al Jawf, and those for Al Hudaydah and Taizz are the lowest.

Table 4.3

Parameter values and confidence intervals for Al Hudaydah

Parameter	Value	95% Confidence Interval
c_1	0.000177	[0, 0.000513]
c_2	0.00905	[0, 0.06278]
c_3	716.95	[0, 23892.8]
c_4	0.007175	[0, 1.030079]
η	0.00000018	[0, 0.00540949]

Table 4.4

Parameter values and confidence intervals for Taizz

Parameter	Value	95% Confidence Interval
c_1	0.000194	[0, 0.000714]
c_2	0.00619	[0, 0.04580]
c_3	2942.27	[0, 33807.6]
c_4	0.013275	[0, 0.754684]
η	0.00000029	[0, 0.00290991]

Based on the parameters estimated in each scenario, we have calculated the two parts $\mathcal{R}_{01}$ and $\mathcal{R}_{02}$ in equation (4.1.5), which represent the contribution from the direct and indirect transmission routes, respectively, to the overall disease risk. We observe that the ratio of $\mathcal{R}_{01}/\mathcal{R}_{02}$ is high for the two governorates in the Northwest and Southwest, showing that the direct transmission route plays the dominant role in

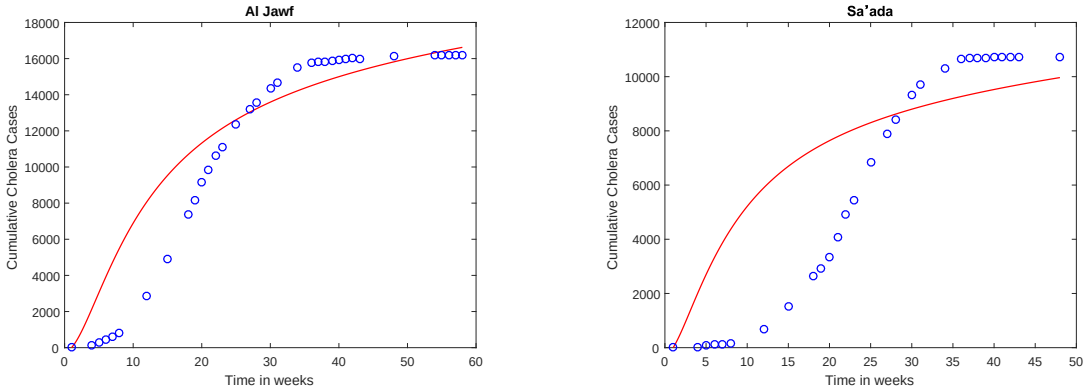

Figure 4.4

Curve fittings for Al Jawf and Sa'ada

shaping the transmission pattern in these places. Particularly, for Al Hudaydah in the Northwest, the value of $\mathcal{R}_{01}$ is almost 8 times of that of $\mathcal{R}_{02}$. On the other hand, for Al Jawf and Sa'ada in the East, the values of $\mathcal{R}_{01}$ and $\mathcal{R}_{02}$ are much closer, indicating that the indirect transmission route plays a more significant role there. A possible explanation for this difference is that in the country of Yemen, the population density in the Northwest and Southwest is much higher than that in the East [65, 72], thus the direct, human-to-human, transmission route may contribute more to the cholera epidemic in the Northwest and Southwest, but less in the East.

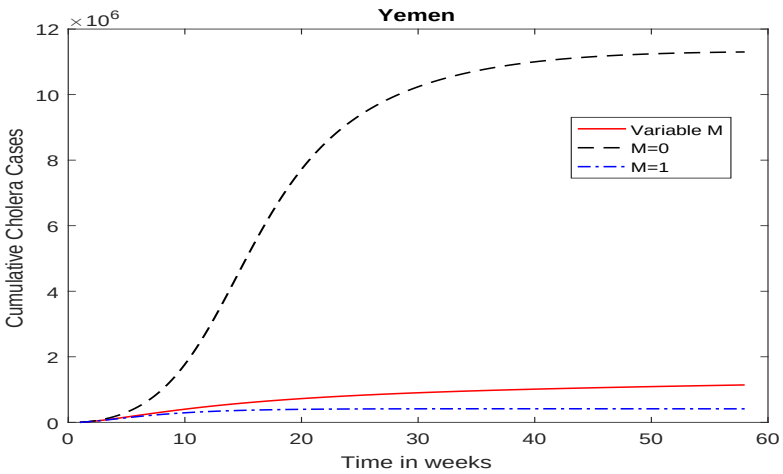

Figure 4.5

Comparison with two hypothetical scenarios: $M = 0$ and $M = 1$

In addition, we have examined the variation of M in our simulation. We find that the value of M is generally decreasing throughout the course of the epidemic, indicating the continuing decline of the available medical resources and deterioration of the public health system due to the conflicts and wars, despite the stimulation from the on-going cholera outbreak. Particularly, we have calculated the value of M_0 , the level of medical resources at the disease-free equilibrium, for these four governorates under consideration (see the caption under each figure). We see that the values of M_0 in Al Hudaydah and Taizz are much higher than those in Al Jawf and Sa'ada, implying that a much higher level of medical resources is required to attain the disease-free state in the Northwest and Southwest regions, than that required in the East region. This is possibly caused by the larger populations (that demand more medical supplies/facilities) and the higher degrees of outbreak severity (characterized by the high levels of prevalence and accumulated cases) in the Northwest and Southwest.

Table 4.5

Parameter values and confidence intervals for Al Jawf

Parameter	Value	95% Confidence Interval
c_1	0.000114	[0, 0.001277]
c_2	0.00772	[0, 0.11596]
c_3	905.93	[0, 87475.7]
c_4	0.006558	[0, 1.811938]
η	0.00033287	[0, 0.04647364]

To further demonstrate the impact of the available medical resources, which interact with the disease transmission dynamics and vary with time, on the Yemen cholera outbreak, we consider two extreme cases with fixed M: $M = 0$ (no resources available throughout the epidemic) and $M = 1$ (100% resources available throughout the epidemic). In each of these two scenarios, the disease transmission rates $\beta_1(M)$ and $\beta_2(M)$, and the rate of human contribution to the bacterial growth, $\xi(M)$, are all reduced to constants; i.e., independent of M. When $M = 0$, the host transmission and pathogen growth rates

Table 4.6

Parameter values and confidence intervals for Sa'ada

Parameter	Value	95% Confidence Interval
c_1	0.000085	[0, 0.003875]
c_2	0.00709	[0, 0.25926]
c_3	1903.02	[0, 339665.7]
c_4	0.005915	[0, 4.052557]
η	0.00040432	[0, 0.10256739]

Table 4.7

The values of $M_0, \mathcal{R}_{01}, \mathcal{R}_{02}$, and $\mathcal{R}_0$ in four governorates

	Al Hudaydah	Taizz	Al Jawf	Sa'ada
M_0	0.262	0.600	0.032	0.014
$\mathcal{R}_{01}$	1.136	0.914	0.814	0.606
$\mathcal{R}_{02}$	0.146	0.218	0.208	0.406
$\mathcal{R}_0$	1.282	1.132	1.022	1.012

are fixed at their maximum values, so that higher disease prevalence and severity are expected. When $M = 1$, these transmission and growth rates remain at their minimum values for the entire course, which would lead to a less severe epidemic. Figure 4.5 plots the numbers of infected human hosts in Yemen for $M = 0$ and $M = 1$, and compare those to the scenario emphasized in our model where M is a variable with respect to the time. An implication of these results is that without considering the impact of the dynamic, time-dependent medical resources, we might either over-estimate or under-estimate the disease risk.

4.3 Discussion

Our model includes both the human-to-human (direct) and environment-to-human (indirect) transmission pathways. In particular, we have incorporated the strength of the medical resources as a key component in the model, on which the transmission rates

explicitly depend. Our model thus represents the interaction among the human hosts (susceptible, infectious, and recovered), the environmental pathogen, and the available medical resources, which shapes the transmission pattern of a cholera epidemic. Moreover, we have carefully analyzed the dynamical properties of our model. Particularly, using the geometric approach based on the third compound matrix, we are able to establish the global asymptotic stability of the endemic equilibrium for our model (which essentially constitutes a four-dimensional system). Our analytical results show that under this model setting, cholera transmission follows regular threshold dynamics that are characterized by the basic reproduction number $\mathcal{R}_0$; i.e., the disease will be eradicated when $\mathcal{R}_0 \leq 1$ and will be persistent when $\mathcal{R}_0 > 1$.

In addition, our model was applied to the simulation of the recent cholera outbreak in Yemen, as a means to demonstrate the application of our model and to verify our analytical predictions. We fit the model parameters using the realistic data published by WHO for both the whole country level and individual governorate level, with a few typical governorates from the three major regions of Yemen (the Northwest, the Southwest, and the East). The findings from our numerical simulation and data fitting show significant differences of transmission structures among the three regions; these are reflected by the degrees of outbreak severity, disease risk quantifications, relative roles played by the direct and indirect transmission routes, and demand levels of medical resources. The results help us to better understand the complex, and heterogeneous, disease dynamics involved in this extremely severe and long-lasting cholera epidemic.

The Yemen cholera outbreak provides a realistic case study for this model, as the high prevalence and severity of this cholera epidemic are widely believed to stem from the collapsed health system and limited medical resources in this country. We obtain reasonably good results in fitting our model to the reported cholera data. Moreover, we find that different degrees of epidemic severity are linked to different geographical regions, which in term leads to different levels of demands for necessary medical resources in order to reach a disease-free state. These findings indicate that cholera prevention/intervention efforts should be implemented strategically with respect to different locations.

CHAPTER 5

CONCLUSION

Our first work in Chapter 2 emphasizes the importance of incorporating the intrinsic bacteria dynamics into mathematical modeling of cholera and the necessity of addressing different types of growth dynamics for different bacteria. In the meantime, our mathematical modeling results could offer useful guidelines to biologists/ecologists with interest in cholera epidemiology and public health professionals in the design of experiments, in the collection of data, and in the efforts of controlling cholera outbreaks.

Then, we have presented a new deterministic modeling framework to link the between-host and within-host dynamics of cholera. The major innovation of our work is the representation of each individual host in a separate manner which allows natural incorporation of host heterogeneities into the within-host dynamics, yet keeping the model mathematically and computationally tractable. Although this model allows the incorporation of heterogeneities from different host individuals, the characterization of the within-host dynamics for each individual is still simple, represented by a single equation for each. Our future work will seek to improve it by incorporating the interactions among the vibrios, cholera toxin phages, and the immune response, so as to gain a deeper understanding of the complex processes of pathogen evolution inside the human body.

In the end, we have formulated a mathematical model to investigate cholera transmission under the impact of limited medical resources. Our work puts an emphasis on the availability of medical resources and its contribution to the overall transmission pattern of cholera. It is well known that the transmission and spread of cholera involve complicated biological, environmental, and socio-economic processes, and the underlying mechanism for a cholera outbreak may vary from place to place. Particularly for Yemen,

stronger control measures should be planned, and more attention should be paid to the reduction of the direct disease transmission, for the Northwest and Southwest regions than that for the East region. Above all, the improvement of public health infrastructure and recovery of medical facilities and supplies are of fundamental importance in fighting future cholera outbreaks.

REFERENCES

[1] W. C. Allee, Animal aggregations: A study in general sociology, *AMS Press*, 1978.

[2] W. C. Allee, A. Emerson, O. Park, T. Park, K. Schmidt, Principles of animal ecology, *Saunders, Philadelphia*, 1949.

[3] J. R. Andrews, S. Basu, Transmission dynamics and control of cholera in Haiti: an epidemic model, *Lancet*, 377(9773): 1248-1255, 2011.

[4] S. Batterman, J. Eisenberg, R. Hardin, et al., Sustainable control of water-related infectious diseases: A review and proposal for interdisciplinary health-based systems research, *Environmental Health Perspectives*, 117: 1023-1032, 2009.

[5] D. Bernstein, Matrix Mathematics, *Princeton University Press*, 2005.

[6] E. Bonabeau, Agent-based modeling: Methods and techniques for simulating human systems, *Proc. Natl. Acad. Sci.*, USA, 99: 7280-7287, 2002.

[7] R. J. Borroto, Ecology of vibrio cholerae serogroup 01 in aquatic environments, *Pan Am. J. Public Health*, 2(5): 328-333, 1997.

[8] C. J. Browne, G. Webb, A nosocomial epidemic model with infection of patients due to contaminated rooms, *Discrete Contin. Dyn. Syst. Ser. B*, 12: 761-787, 2015.

[9] L. Cai, C. Modnak, J. Wang, An age-structured model for cholera control with vaccination, *Appl. Math. Comput.*, 229: 127-140, 2017

[10] L. Cai, N. Tuncer, M. Martcheva, How does within-host dynamics affect population-level dynamics? Insights from an immuno-epidemiological model of malaria, *Math. Methods Appl. Sci.*, 40: 6424-6450, 2017.

[11] A. Camacho, M. Bouhenia, R. Alyusfi, et al., Cholera epidemic in Yemen, 2016-18: an analysis of surveillance data, *Lancet Global Health*, published online, May 3, 2018. http://doi.org/10.1016/S2214-109X(18)30230-4

[12] V. Capasso, S. L. Paveri-Fontana, A mathematical model for the 1973 cholera epidemic in the European Mediterranean region. *Rev. Epidemiol. Sante*, 27(2): 121-132, 1979.

[13] R. R. Colwell, A global and historical perspective of the genus Vibrio, in *The Biology of Vibrios*, F.L. Thompson, B. Austin, J. Swings (eds.), *ASM Press, Washington DC*, 2006.

[14] F. Courchamp, T. Clutton-Brock, B. Grenfell, Inverse density dependence and the allee effect, *Trends Ecol. Evol.*, 14: 405-410, 1999.

[15] S. Cumberland, An old enemy returns, *Bulletin of the World Health Organization*, 87: 85-86, 2009.

[16] J. M. Cushing, Backward bifurcations and strong allee effects in matrix models for the dynamics of structured populations, *J. Biol. Dyn.*, 8(1): 57-73, 2014.

[17] J. M. Cushing, J. T. Hudson, Evolutionary dynamics and strong allee effects, *J. Biol. Dyn.*, 6(2): 941-958, 2012.

[18] B. S. Drasar, B. D. Forrest Eds., Cholera and the ecology of vibrio cholerae, *Springer: Netherlands*, 1996.

[19] M. C. Eisenberg, Z. Shuai, J. H. Tien, P. van den Driessche, A cholera model in a patchy environment with water and human movement, *Math. Biosci.*, 246: 105-112, 2013.

[20] S. M. Faruque, M. J. Albert, J. J. Mekalanos, Epidemiology, genetics, and ecology of toxigenic vibrio cholerae, *Microbiol. Mol. Biol. Rev.*, 62: 1301-1314, 1998.

[21] S. M. Faruque, G. B. Nair, Vibrio cholerae: Genomics and Molecular Biology, *Caister Academic Press*, 2008.

[22] O. Felsenfeld, The survival of cholera vibrios, in: D. Barua, W. Burrows (Eds.), *Cholera, Saunders, Philadelphia*, 359-366, 1974.

[23] A. Friedman, A.-A. Yakubu, Fatal disease and demographic allee effect: population persistence and extinction, *J. Biol. Dyn.*, 6(2): 495-508, 2012.

[24] D. Gao, S. Ruan, An SIS patch model with variable transmission coefficients, *Math. Biosci.*, 232: 110-115, 2011.

[25] H. Gulbudak, M. Martcheva, Forward hysteresis and backward bifurcation caused by culling in an avian influenza model, *Math. Biosci.*, 246(1): 202-212, 2013.

[26] A. B. Gumel, Causes of backward bifurcations in some epidemiological models, *J. Math. Anal. Appl.*, 395(1): 355-365, 2012.

[27] D. M. Hartley, J. G. Morris, D. L. Smith, Hyperinfectivity: a critical element in the ability of *V. cholerae* to cause epidemics? *PLoS Med.*, 3: 0063-0069, 2006.

[28] D. He, X. Wang, D. Gao, and J. Wang, Modeling the 2016-2017 Yemen cholera outbreak with the impact of limited medical resources, *Journal of Theoretical Biology*, 451: 80-85, 2018.

[29] G. E. Hutchinson, An introduction to population ecology, *Yale University Press*, 1978.

[30] G. Ji, R. C. Beavis, R .P. Novick, Cell density control of staphylococcal virulence mediated by an octapeptide pheromone, *Proc. Natl. Acad. Sci.*, 92: 1205512059, 1995.

[31] S. V. Kadam, G. J. Velicer, Variable patterns of density- dependent survival in social bacteria, *Behav. Ecol.*, 17(5): 833-838, 2006.

[32] Y. Kang, S. K. Sasmal, A. R. Bhowmick, J. Chattopadhyay, A host-parasitoid system with predation-driven component allee effects in host population, *J. Biol. Dyn.*, 9: 213-232, 2015.

[33] A. M. Kramer, B. Dennis, A. M. Liebhold, J. M. Drake, The evidence for allee effects, *Popul. Ecol.*, 51: 341-354, 2009.

[34] J. P. LaSalle, The Stability of Dynamical Systems, Regional Conference Series in Applied Mathematics, *SIAM, Philadelphia*, 1976.

[35] Y. Li, M. Hanna, G. Svensater, R. Ellen, D. Cvitkovitch, Cell density modulates acid adaptation in streptococcus mutans: implications for survival in biofilms, *J. Bacteriol.*, 183: 6875-6884, 2001.

[36] M. Y. Li, J. S. Muldowney, A geometric approach to global-stability problems, *SIAM J. Math. Anal.*, 27: 1070-1083, 1996.

[37] M. Y. Li, J. S. Muldowney, and P. V. D. Driessche, Global stability of SEIRS models in epidemiology, *Canadian Applied Mathematics Quarterly*, 7: 409-425, 1999.

[38] P.R. Mason, Zimbabwe experiences the worst epidemic of cholera in Africa, *Journal of Infection in Developing Countries*, 3: 148-151, 2009.

[39] E. D. Mintz and R. V. Tauxe, Cholera in Africa: a closer look and a time for action, *Journal of Infectious Diseases*, 208(S1): S4-7, 2013.

[40] Z. Mukandavire, S. Liao, J. Wang, H. Gaff, D. L. Smith, J. G. Morris, Estimating the reproductive numbers for the 2008-2009 cholera outbreaks in Zimbabwe, *P. Nat. Acad. Sci.*, USA, 108: 8767-8772, 2011.

[41] R. L. M. Neilan, E. Schaefer, H. Gaff, K. R. Fister, S. Lenhart, Modeling optimal intervention strategies for cholera, *Bull. Math. Biol.*, 72: 2004-2018, 2010.

[42] E. J. Nelson, J. B. Harris, J. G. Morris, S. B. Calderwood, A. Camilli, Cholera transmission: the host, pathogen and bacteriophage dynamics, *Nat. Rev. Microbiol.*, 7: 693-702, 2009.

[43] M. Niazi and A. Hussain, Agent-based computing from multi-agent systems to agent-based models: A visual survey, *Scientometrics*, 89: 479-499, 2011.

[44] D. Posny, J. Wang, Modelling cholera in periodic environments, *J. Biol. Dyn.*, 8(1): 1-19, 2014.

[45] H. Rahmandad and J. Sterman, Heterogeneity and network structure in the dynamics of diffusion: Comparing agent-based and differential equation models, *Manag. Sci.*, 54(5): 998-1014, 2008.

[46] S. Shin, S. N. Desai, B. K. Sah, J. D. Clemence, Oral vaccines against cholera, *Clinical Infectious Diseases*, 52(11): 1343-1349, 2011.

[47] Z. Shuai, P. van den Driessche, Global stability of infectious disease models using Lyapunov functions, *SIAM J. Appl. Math.*, 73(4): 1513-1532, 2013.

[48] C. I. Siettos and L. Russo, Mathematical modeling of infectious disease dynamics, *Virulence*, 4(4): 295-306, 2013.

[49] R. Smith, C. Tan, J. K. Srimani, A. Pai, K. A. Riccione, H. Song, L. You, Programmed allee effect in bacteria causes a tradeoff between population spread and survival, *Proc. Natl. Acad. Sci.*, 111: 1969-1974, 2014.

[50] G.-Q. Sun, Mathematical modeling of population dynamics with Allee effect, *Nonlinear Dyn.*, 85: 1-12, 2016.

[51] H. R. Thieme, Persistence under relaxed point-dissipativity (with application to an endemic model), *SIAM J. Math. Anal.*, 24: 407-435, 1993.

[52] J. P. Tian, J. Wang, Global stability for cholera epidemic models, *Math. Biosci.*, 232(1): 31-41, 2011.

[53] J. H. Tien, D. J. D. Earn, Multiple transmission pathways and disease dynamics in a waterborne pathogen model, *B. Math. Biol.*, 72(6): 1506-1533, 2010.

[54] A. R. Tuite, J. H. Tien, M. C. Eisenberg, D.J.D. Earn, J. Ma, D. N. Fisman, Cholera epidemic in Haiti, 2010 – using a transmission model to explain spatial spread of disease and identify optimal control interventions, *Annals of Internal Medicine*, 154: 593-601, 2011.

[55] P. van den Driessche. J. Watmough, Reproduction numbers and sub-threshold endemic equilibria for compartmental models of disease transmission, *Math. Biosci.*, 180: 29-48, 2002.

[56] X. Wang, D. Gao, J. Wang, Influence of human behavior on cholera dynamics, *Math. Biosci.*, 267: 41-52, 2015.

[57] J. Wang, S. Liao, A generalized cholera model and epidemic-endemic analysis, *J. Biol. Dyn.*, 6(2): 568-589, 2012.

[58] X. Wang, J. Wang, Analysis of cholera epidemics with bacterial growth and spatial movement, *J. Biol. Dyn.*, 9(1): 233-261, 2015.

[59] X. Wang and J. Wang, Disease dynamics in a coupled cholera model linking within-host and between-host interactions, *J. Biol. Dyn.*, 11: 238-262, 2017.

[60] X. Wang, J. Wang, Modeling the within-host dynamics of cholera: Bacterial-viral interaction, *J. Biol. Dyn.*, 11: 484-501, 2017.

[61] C. Yang, D. Posny, F. Bao, J. Wang, A multi-scale cholera model linking between-host and within-host dynamics, *International Journal of Biomathematics*, 11(3): 1850034, 2018.

[62] C. Yang, J. Wang, A cholera transmission model incorporating the impact of medical resources, *Mathematical Biosciences and Engineering*, 16(5): 5226-5246, 2019.

[63] C. Yang, J. Wang, On the intrinsic dynamics of bacteria in waterborne infectious, *Mathematical Biosciences*, 296: 71-81, 2018.

[64] G. Zorlu, Cholera vaccine deployed to control African outbreak, *Nature*, News and Comment, June 2012.

[65] Climate and Average Weather in Yemen: http://weather-and-climate.com/average-monthly-Rainfall-Temperature-Sunshine-in-Yemen

[66] WHO cholera fact sheet: 1 February 2018. http://www.who.int/en/news-room/fact-sheets/detail/cholera

[67] WHO Global health observatory data repository: Life expectancy, 2013. http://apps.who.int/gho/data/view.main.680?lang=en

[68] WHO report on global surveillance of epidemic-prone infectious diseases, 39-54, 2000.

[69] WHO survey on Yemen's health system: http://www.emro.who.int/media/news/survey-reveals-extent-of-damage-to-yemens-health-system.html

[70] WHO Weekly Epidemiology Bulletin, 21-27, May 2018.

[71] WHO Yemen cholera situation reports: http://www.emro.who.int/yem/yemenin focus/situation-reports.html

[72] Wikipedia page for Yemen: http://en.wikipedia.org/wiki/Yemen

[73] World Climate Guide: http://www.climatestotravel.com/climate/yemen

VITA

Chayu Yang was born in Pengzhou, Sichuan, China, to parents Yuantong Yang and Wenliang Tang. He is their only child. He attended Hongmiao Elementary School, then Nanyang High School and continued to Pengzhou High School, where he became interested in mathematics in Pengzhou, Sichuan. After graduation, he attended the University of Science and Technology of China, where he completed his Bachelor's degree in Statistics and Master of Science degree in Mathematics in June 2009 and June 2012, respectively. In addition, he obtained his Master of Science degree in Computational and Applied Mathematics in August 2017 at The University of Tennessee at Chattanooga. Chayu Yang is continuing his education in Applied Mathematics by pursuing the Ph.D. degree in Computational Science at The University of Tennessee at Chattanooga.